DOI:
10.1016/j.rse.2018.08.015

Document Version
Peer reviewed version

Investigating the impact of overlying vegetation canopy structures on fire radiative power (FRP) retrieval through simulation and measurement

Roberts, G[1]*, Wooster, M. J[23]., Lauret, N[4]., Gastellu- Etchegorry, J-P[4]., Lynham, T[5]. and McRae, D[5].

*corresponding author

1) Geography and Environment, University of Southampton, Southampton, UK

2) Kings College London, Department of Geography, London, UK, WC2R 2LS.

3) NERC National Centre for Earth Observation (NCEO), Kings College London, UK

4) CESBIO, Toulouse University, CNES, CNRS, IRD, UPS (Toulouse),France

5) Canadian Forest Service, Great Lakes Forestry Centre, 1219 Queen Street East, Sault Ste. Marie, ON, Canada

Abstract

Fire radiative power (FRP) retrievals are now routinely made from polar and geostationary instruments, providing a means to estimate fuel consumption and trace gas and aerosol emissions directly from remotely sensed observations. This study presents the first investigation of the impact of vegetation canopy structure (percentage canopy cover and leaf area index, LAI) on FRP measurements, based on 3D radiative transfer model simulations. The Discrete Anisotropic Radiative Transfer (DART) model is used to simulate above-canopy observations made through 3D vegetation canopies with different structural arrangements, under which a centrally positioned uniform landscape fire is burning. The vegetation canopy is modelled in

two ways, as an opaque structure and as a hybrid turbid medium. The percentage canopy cover in each simulated scene is varied between 5-95%, and the FRP retrieved above the canopy is found to decrease in proportion to percentage canopy cover when the canopy is opaque, a finding that is in agreement with a series of small scale outdoor measurements conducted to evaluate the realism of the simulations. However, when the canopy is modelled as a turbid medium, which is in some ways a more realistic representation of a real 'gappy' vegetation canopy, the degree of FRP interception occurring at any particular canopy cover decreases by ~ 14%, due to some fire emitted thermal energy being transmitted through the canopy gaps. The simulations also reveal the impact of canopy LAI on above-canopy FRP measures, reducing these by 6% when both canopy cover and LAI are low (5% and <1.0 respectively) are low, but by up to 92% when canopy cover and scene LAI are high (95% and ~8 respectively). We use the derived relationships between FRP interception and canopy structure, along with MODIS LAI and percentage tree cover data, to adjust 2004-2012 fire radiative energy (FRE) estimates calculated from FRP data collected by the geostationary Meteosat Spinning Enhanced Visible and Infrared Imager (SEVIRI) instrument. The adjusted annual FRE is on average 15% greater than measured, and is characterized by low inter-annual variability as result of the majority of fire activity occurring in areas where percentage tree cover remains below 40%. Landscape burning occurs more frequently in areas of higher tree cover in southern hemisphere rather than northern hemisphere Africa, leading to a larger annual FRE adjustment (18.5% compared to 16.3%). This study illustrates the impact that canopy interception has on FRP for the first time at the satellite scale, and over Africa demonstrates a large but temporally consistent underestimation which can be accounted for using LAI and percentage tree cover metrics when estimating fuel consumption and atmospheric emissions from the FRP retrievals.

2. Introduction

Landscape fire is a global, highly dynamic Earth system process, altering surface structural and radiative properties and releasing aerosols and trace gases into the atmosphere (Arora and Boer, 2005; Bowman *et al.*, 2009). Satellite Earth Observation (EO) has been widely applied to study landscape fires, either through measurements of burned area based on surface spectral reflectance change (Pereira, 1999; Giglio *et al.*, 2013), or via the detection of the thermal energy radiated as the fire burns (Robinson, 1991; Zhukov *et al.,* 2005; Xu *et al.*, 2010). The 'active fire' approach uses thermal infrared observations to estimate the rate at which thermal energy is being radiated away from a fire (the fire radiative power). Retrievals of FRP are then used to back-calculate the rate of fuel consumption that must have been ongoing to produce the observed rate of thermal radiant energy release (Kaufman *et al.*, 1996). Small scale experiments have shown strong links between the temporal integral of FRP (so-called Fire Radiative Energy; FRE) and fuel consumption that appear to be independent of vegetation type (Wooster *et al.*, 2005). Landscape fire fuel consumption is most typically derived using burned area (Chuvieco *et al.*, 2016; Giglio *et al.,* 2013) or FRE (Ellicott *et al.*, 2009; Kaiser *et al.,* 2012) based methods, and we focus here on canopy cover impacts on the latter approach and the resulting effect this may have on the information derived from satellite-based FRP retrievals. Numerous studies have utilized FRP retrievals from polar-orbiting (e.g. Vermote *et al.*, 2009; Andela *et al.,* 2016; Schroeder *et al.*, 2014) and geostationary sensors (e.g. Ellicott *et al.,* 2008; Li *et al.,* 2018; Mota and Wooster, 2018) to estimate fuel consumption, and/or smoke emissions, and in terms of fuel consumption many have typically been lower than those from burned area based approaches (Roberts *et al.,* 2011), and also lower than expected from ground-based measures (Andela *et al.*,

2016). A variety of factors may contribute to this apparent underestimation, and to the uncertainty of FRE measures more generally, for example satellite orbital constraints that limit the number of FRP observations in a given time-period (Andela *et al.*, 2015), sensor optical characteristics (e.g. spatial resolution, point spread function and sensor saturation; Calle *et al.,* 2009; Wooster *et al.,* 2015), active fire detection algorithm performance (Giglio *et al.*, 2016, Freeborn *et al.,* 2014b) and FRP measurement random error (Boschetti and Roy, 2009; Freeborn *et al.,* 2014a). Vegetation canopy cover masking some of the emitted FRP from view is a further possible and potentially highly significant effect that has so far not been quantitatively studied. We focus on this issue herein, which typically does not affect burned area based estimates of fuel consumption unless the canopy cover results in special approaches being required to identify sub-canopy burned areas (e.g. in thick forests; Morton *et al.*, 2011). A further key advantage of the burned area based approach to fuel consumption estimation is that this method enables identification of short duration fires which may be missed by active fire methods, which is important as it is typically the omission of these fires which is a significant source of FRP underestimation (e.g. Roberts and Wooster, 2008; Zhukov *et al.,* 2006; Freeborn *et al.,* 2014b; Zhang *et al.*, 2017). However, on the other hand, burned area based approaches to total fuel consumption estimation require separate information on fuel consumption per unit area within the burn scar to be provided, which is often difficult to obtain for particular fire-affected locations (van Leeuwen *et al.*, 2014). Recent studies based on satellite-derived FRPs have also suggested a biome-dependence in the relationship between FRP and fuel consumption that remains unexplained (Kaiser *et al.,* 2012; Schroeder *et al.,* 2014; Li *et al.,* 2018). Spaceborne retrievals of FRP are made through the full depth of the atmosphere and through any overlying vegetation canopy that may lie above a surface fire, and these may be

responsible for some of the biome-dependence on the FRP-to-fuel consumption relations noted when using spaceborne observations (Kremens *et al*., 2012; Mathews *et al.,* 2016; Mota and Wooster; 2018).

We investigate the canopy cover impact on FRP and FRE measures using a 3D radiative transfer model. Such models provide key tools for understanding interactions between solar and terrestrially emitted VIS to LWIR radiation and Earth's surface and atmosphere, including the elucidation of atmospheric effects on the measured remotely sensed signals. Radiative transfer models have been applied to simulate fire impacts on surface spectral properties (Disney *et al.,* 2011), to develop algorithms to quantify fire impacts on the land surface from such signals (Chuvieco *et al*., 2006), and to characterise the detectability of burned areas occurring under forest canopies (Pereira *et al.,* 2004). Here we use the Discrete Anisotropic Radiative Transfer (DART) model (Gastellu-Etchegorry *et al*., 1996) to simulate the thermal 3D radiative transfer within and above landscapes to investigate canopy impacts on FRP, and to understand the degree to which spaceborne observations of surface fire FRP may be influenced by overlying canopy interception.

3. FRP Background

Vegetation is comprised mainly of cellulose, hemi-cellulose, proteins, lignin and water (Stott, 2000), and is approximately 50% carbon by dry mass (Grigal and Ohmann, 1992). During complete combustion the carbon is oxidized to CO_2, with the concomitant release of water vapour, and thermal energy. The heat of combustion ($MJ.kg^{-1}$) represents the total energy available for release upon burning completely in oxygen, and this figure is rather constant between vegetation types, with a minimum

of around 16.2 MJ kg^{-1} for senesced grass and a maximum of around 23.7 MJ kg^{-1} for oil-rich eucalyptus leaves (Jenkins *et al.,* 1998; Johnson, 1992; Stott, 2000). The radiative component of this heat yield can be measured via remote sensing, and the rate of emission of this from a fire containing multiple thermal components, each having different temperatures and areas, is the fire radiative power (FRP, Watts):

$$FRP_{true} = \varepsilon\sigma \sum_{n=1}^{N} A_n T_n^4 \qquad [1]$$

where FRP_{true} is the fire radiative power (Wm^{-2}), N is the number of temperature components in the fire, σ is the Stefan-Boltzmann constant ($5.67x10^{-8}$ J s^{-1} m^{-2} K^{-4}), ε is fire graybody emissivity, A_n is the fractional area and T_n is the temperature of the n^{th} thermal component (K). An important assumption in Equation 1 is that flame behaves as a graybody (i.e. constant emissivity with wavelength). Johnston *et al.* (2013) provide a recent assessment of flame LWIR and MWIR spectral emissivity, and confirm that the graybody assumption is valid (and that flame emissivity increases with flame depth). They also suggest that the absolute value of flame emissivity at any particular flame depth varies with soot volume fraction, whilst the depth as viewed by a remote sensing instrument depends on the viewing geometry and the flame geometry.

Kaufman *et al.* (1998) first suggested the use of FRP retrievals to back calculate smoke emission and fuel consumption rates, and the link between the two has since been quantified in numerous studies (e.g. Wooster *et al.*, 2005; Freeborn *et al.,* 2008; Pereira *et al.,* 2011; Kremens *et al.,* 2012; Smith *et al.,* 2013). Fire radiative energy (FRE; Joules) is the temporal integral of FRP, and the type of linear relationship between FRE and fuel consumption shown by Wooster *et al.* (2005) and

153 Kremens *et al.* (2012) has been exploited with both polar-orbiting and geostationary
154 satellites to estimate the amount of dry matter consumed and the smoke emissions
155 released by landscape fires (Polar Orbiting: e.g. Ichoku and Kaufman, 2005; Ellicott
156 *et al.*, 2009; Vermote *et al.*, 2008; Freeborn *et al.*, 2009; Kaiser *et al.,* 2012;
157 Schroeder *et al.,* 2014; Boschetti and Roy, 2009; Pereira *et al.*, 2009; Geostationary:
158 e.g. Andela *et al.*, 2016; Mota and Wooster, 2018; Roberts *et al.*, 2005, 2011; Zhang
159 *et al.*, 2012; Roberts *et al.*, 2015; Li *et al.*, 2018; Baldassarre *et al.,* 2015).

160 The FRE approach a more direct route to estimating landscape scale fuel
161 consumption than burned area based methods, which still require estimates of fuel
162 load per unit area and combustion completeness from models or field data (e.g.
163 Korontzi *et al.,* 2004; Ito and Penner, 2004; Lehsten *et al.,* 2008; van der Werf *et al.*,
164 2010; Randerson *et al.,* 2012). Whilst FRP retrievals from the MODIS sensor
165 onboard the Terra and Aqua satellites are used for routine fuel consumption and fire
166 smoke emissions calculations however, the linear FRE-to-fuel consumption
167 relationship derived by Wooster *et al.* (2005) during small scale experiments have
168 tended to strongly underestimate landscape scale fuel consumption when applied to
169 these data (Roberts *et al.,* 2011; Andela *et al.*, 2016). This is expected to be
170 particularly significant in more forested regions (Kaiser *et al.*, 2012), and it is
171 assumed to occur as a result of infrared radiation emitted from the surface fires being
172 intercepted by the overlying tree canopy. Additional interception of the above canopy
173 radiation may also come from atmospheric absorption, and these two effects alone
174 may mean that spaceborne FRP retrievals of surface vegetation fires burning below
175 tree canopies maybe significantly lowered compared to what under-canopy
176 observations would provide.

177 Recent studies have investigated certain fuel characteristics that impact the
178 retrieval of FRP. Smith *et al.* (2013) found that fuel moisture reduced the amount of

179 energy released per unit of fuel consumed (MJ. kg^{-1}), up to a maximum of ~25% at
180 the highest vegetation moisture contents (14% moisture content). Using a similar
181 small-scale measurement approach, Mathews *et al.* (2016) investigated the impact of
182 vegetation percentage cover, finding that it reduced FRP in direct linear proportion
183 to the areal coverage of the overlying vegetation. This suggests both that vegetation
184 may be opaque at the thermal IR wavelengths concerned, and that a proportion of
185 the FRP emitted by surface fires will be blocked by this process. Here, we go beyond
186 this laboratory experiment, and explore the landscape scale impact of overlying tree
187 canopies on surface vegetation fires via simulations that include a 3D landscape of
188 fire and vegetation. We explore how the tree canopies may block a certain proportion
189 of the fire-emitted infrared radiation from a spaceborne sensor, and also how
190 different vegetation structures may result in increasingly non-lambertian behaviour
191 in the observed FRP fields. We supplement this with an assessment of the relative
192 importance in controlling the biome-dependent differences seen in FRP-to-fuel
193 consumption relations.
194
195 **4. The Discrete Anisotropic Radiative Transfer (DART) model**
196 We use the DART 3D radiative transfer model to simulate three dimensional
197 Earth-surface scenes at visible to thermal infrared wavelengths (Gastellu-Etchegorry
198 *et al.*, 1996). DART simulations are based on either ray tracing or discrete ordinates
199 methods (Grau and Gastellu-Etchegorry, 2013; Gastellu-Etchegorry *et al.,* 2015). For
200 thermal IR wavelengths, emission of individual surface elements is modelled using
201 the Planck or Stefan Boltzmann Laws and is assumed to be isotropic (Gullevic *et al.*,
202 2003). The resulting representations enable analysis of the Bidirectional Reflectance
203 Distribution Function (BRDF) and Bidirectional Temperature Distribution Function

(BTDF) of the scene to be derived from the simulations, as shown for example by Kallel and Gastellu-Etchegorry (2017) and Gullevic *et al.* (2003).

DART is capable of simulating atmospheric radiative transfer at the surface and in the atmosphere, so in addition to canopy interception can also be used to quantify the impact of atmospheric attenuation on spaceborne FRP observations, including accounting for Earth-atmosphere radiative coupling. Grau and Gastellu-Etchegorry (2013) provide a detailed description of the atmospheric model within DART, and it is only briefly summarized here. The DART atmosphere is simulated using up to three vertical slabs; (1) the upper atmosphere composed of horizontal layers, (2) the middle atmosphere composed of higher resolution vertical and horizontal cells, and (3) a lower atmosphere having the same vertical and horizontal cell dimensions as those used to simulate Earth surface objects. Atmospheric cells are characterized by trace gas and aerosol particle densities, along with their respective optical properties (extinction coefficients and single scattering albedo). DART contains six predefined atmospheric representations taken from the widely used MODerate resolution atmospheric TRANsmission (MODTRAN) model (Berk *et al.,* 2005), for example Midlatitude summer, Sub-Arctic Winter etc, along with a series of aerosol models (e.g. rural 25km visibility, urban 5km visibility).

DART simulates the near-surface of a 3D scene as an array of rectangular cells having a defined spatial cell size. Three dimensional objects, such as trees and buildings, can be simulated using plane surfaces (triangles and parallelograms) or as turbid media. Turbid cells can be used to simulate vegetation (e.g. leaves, woody material) or fluids (e.g. air, soot, water) using defined statistical distributions in which radiation attenuation is described using Beer's Law (Ross, 1981). Surface cells composed of triangles are used to simulate solid objects, such as walls and roofs, vegetation trunks and branches and the materials at the surface (e.g. soils).

Vegetation canopies can be described using turbid cells, facet cells or combinations of both. DART can both import landscape elements (e.g. trees, buildings) or directly simulate them using schematic shapes. For example, DART created tree crowns can be described using pre-defined shapes (e.g. ellipsoid, trapezoid cone) filled with a turbid medium or facets with any dimension can be randomly distributed within the scene or with a pre-defined spatial distribution. Figure 1 illustrates a tree, simulated by DART as part of the RAMI-4 radiative transfer intercomparison exercise (Widlowski *et al.*, 2013), using a combination of turbid grid cells for leaves and opaque triangles for the trunk and branches (Figure 1b) which is derived from the tree model where leaves are described as individual scattering elements (Figure 1c). Turbid cells are described using an infinite number of infinitely small plane surfaces whose 3D distribution is described by the leaf and twig angle distribution, leaf area index (m^2/m^2) or leaf area density (u_f; m^2/m^3) and twig area index (TAI, m^2/m^2). In a schematic tree crown, the vertical and horizontal distribution of leaves and holes (empty cells) can be varied to simulate within crown clumping and defoliation. Cells in a scene have defined optical and thermal properties for each wavelength or spectral band simulated. The optical properties of vegetated cells are described by reflectance and direct and diffuse transmittance profiles, whilst the cells' thermal properties are described by emissivity and temperature. Depending on cell dimensions and on the number of triangles that are used to simulate a tree, the transformation of the 'triangle tree' into 'turbid tree' can decrease computer time while maintaining model accuracy for computing the tree canopy optical properties. This transformation allows one to retain the general tree 3D architecture, conversely to the use of trees that are simulated with schematic crown shapes. This point is important when considering the transmittance of tree canopies. DART provides a range of outputs including 2D arrays representing the

spatial distribution of spectral radiance, bidirectional reflectance factor (BRF) and brightness temperature (BT), including for each wavelength or spectral band and viewing geometry simulated.

The flexibility provided by DART has seen it applied to simulate the radiative regime of heterogeneous 3D vegetation canopies in the visible (Malenovsky *et al.,* 2008; Sepulcre-Canto *et al.,* 2009; Schneider *et al*., 2014) and thermal (Guillevic *et al.,* 2003; Sepulcre-Canto *et al.,* 2009) domains and urban areas (Lagouarde *et al.,* 2010; 2012). DART was also used in the RAdiation transfer Model Intercomparison (RAMI; Widlowski *et al*., 2007; 2008) exercise, and was shown to have very similar performance in the visible and near infrared (NIR) to other 3D RT models. Sobrino *et al.* (2011) compared DART simulated scenes against ground, airborne and spacebone (Advanced Spaceborne Thermal Emission and Reflection Radiometer; ASTER) imagery in the LWIR spectral (8-13 μm), indicating the DART simulations had an absolute RMSE < 2K when compared to ground radiometric temperature measurements. Lagouarde *et al.* (2010) used DART to model the LWIR BTDF of an urban area and also found generally good agreement between simulated and observed temperatures, with the error bounds identified by these other studies. Though DART has been widely validated in the VIS to SWIR and LWIR spectral region (e.g. Gastellu-Etchegorry *et al.,* 2015; Kallel *et al.,* 2017; Morton *et al.,* 2016; Laguarde *et al.,* 2012), its abilities within the middle infrared (MWIR) are yet to be fully assessed.

5. Methodology to simulate canopy effects on FRP retrieval

5.1 DART Setup

A series of DART 3D simulations were conducted in the MODIS MWIR spectral waveband (Band 21; 3.929-3.989 μm), which is the primary waveband

used for both active fire detection and FRP retrieval in the official MODIS active fire products (Giglo *et al.,* 2016). To investigate canopy interception of upwelling surface fire-emitted radiation, a 50m × 50m scene was simulated at a 0.25 m spatial resolution, with each simulation covering 500 different viewing directions (0-80° view zenith and 0-360° view azimuth angles. A fixed solar zenith (30°) and azimuth (225°) angle were assumed since the focus of the study concerns the impact of overlying vegetation on FRP retrieval.

Scene cells had defined optical (i.e. hemispherical directional reflectance and transmittance) and thermal properties, parametrised according to their material type. Ground surface temperature was set to 310 K and its optical properties set to that of a gravelly loam soil (Figure 1a). For this material, scattering in the 3-5 μm wavelength range is dominated by the fine grain size and mineral composition (Salisbury and D'Aria, 1994; Boyd and Petitcolin, 2004).

A fire was positioned centrally in each scene and covering a planimetric area of the surface 25 m × 25 m in size. Whilst the flames present during vegetation combustion can have complex radiative characteristics within parts of the MWIR (3-5 μm) spectral region, resulting from spectral emission by e.g. hot CO_2 and water vapour, the narrow (3.929-3.989 μm) MODIS Band 21 that is used for FRP retrieval was specifically designed to lie outside most gaseous absorption and emission regions (Kaufman *et al.,* 1998), and so the vast majority of the fires' thermal radiant energy emissions in this spectral band come from the hot combusting fuel bed (Parent *et al.*, 2010). Since our primary interest was simulating the impact of canopy radiation interception on MODIS-estimated FRP retrievals, we therefore simulated the fire as a flat (Lambertian), high temperature surface located at ground level. This simplification neglects the spectral variation of the thermal radiation emitted by

307 combustion products within the flames (e.g. soot, CH_4, CO, CO_2 and H_2O) that may
308 occur within the MWIR waveband.

309 Temperatures found at actively combusting vegetation sites range from 600 to
310 1100 K (Dennison *et al.*, 2006), and we selected a uniform brightness temperature of
311 1000K for our simulation. At this temperature, the approximations used within the
312 MIR radiance method of FRP retrieval, as used in the MODIS fire products for
313 example, have negligible impact on FRP bias (Wooster *et al.*, 2003). This allowed us
314 to focus on the biases introduced by vegetation interception of the upwelling thermal
315 radiation, and our simplification of a real vegetation fire situation is sufficient to
316 assess the impact of vegetation canopy structure on FRP retrieval.

317 Trees surrounding and overlying the fire were modelled using a 2.3m width,
318 2.3m length and 2.8m height tree model (Figure 1b), which are appropriate physical
319 dimensions relative to the dimensions of the simulated scene. In each tree, turbid
320 cells containing leaf material were described using the optical properties of green
321 deciduous leaves. Their emissivity varies somewhat with water content, being higher
322 during dry, senescent periods (Salisbury and D'Aria, 1994; Monod *et al.*, 2009), but
323 in general leaf reflectivity and transmissivity are both uniformly low across the 3-5
324 μm wavelength range (0.9-2.5% and 0.6-1.7% respectively), with the exception of
325 reststrahlen reflectance peaks at 3.44 μm and 3.52 μm (Salisbury and D'Aria, 1994).
326 The former optical properties were all obtained from the DART spectral library, but
327 those of the tree's woody material (i.e. trunks and branches) were taken from the
328 University of California Santa Barbara Emissivity Library
329 (www.icess.ucsb.edu/modis/EMIS/html/em.html), where the spectral reflectance of
330 eucalyptus bark was used, this being higher than green leaf material (mean of 18%)
331 in the MWIR spectral region due to the effect of surface texture on scattering
332 (Salisbury and D'Aria, 1994). Infrared transmittance was assumed to be zero for

these fully opaque components, which were simulated using opaque cylinders. The trees leaves and woody material were assigned surface temperatures of 300 K and 295K respectively, whilst the surrounding atmosphere was assigned a value of 300K. A sensitivity analysis of this parameter indicates its impact on FRP retrievals is minimal (<<0.01 % change when atmospheric temperature reduced to 220K). Table 1 outlines the parameters used to describe the scene and scene objects in the DART simulations.

5.2 Simulation Approaches

The leaf angle distribution (LAD) describes the angle between the leaf surface normal and the view zenith, and is a key parameter characterising radiative transfer through a vegetation canopy, described by the gap frequency model (Nilson, 1971). To select a representative leaf angle distribution (LAD) for the turbid medium simulations, and to assess the impact of changing LAD on the interception of FRP by the canopy, a simulation of a horizontally homogeneous vegetation canopy was varied to include uniform, spherical, erectophile, planophile, extremeophile, plagiophile, horizontal and vertical LAD functions. The canopy leaf area index (LAI, $m^2.m^{-2}$), which describes the ratio of the one-sided leaf surface area to ground area, was set to 2.0 in each of these simulations, and Figure 2 shows the results. LAD choice can clearly have a large impact on the degree of canopy interception of FRP, and at extreme view zenith angles (>70°) most LAD functions result in a large FRP deficit compared to the no canopy situation. When viewing at nadir, the largest differences are found between the horizontal and vertical LADs (Fig. 2g and 2h respectively). However, whilst significant differences can exist in the FRP measured between different LAD simulations at any particular view zenith angle, differences in the total FRP observed above canopy is typically less than 4% (with the exception of

359 horizontal and vertical leaf angle distributions, which differ by ~ 9%). All subsequent
360 simulations were conducted with a spherical LAD because this is the most widely
361 assumed in modelling canopy radiative transfer (Pisek *et al.*, 2013) and because it
362 has a statistically uniform distribution of leaf directions.

363 To reduce computational load, simulated leaves from the discrete element
364 simulation (Figure 1c) were converted to a turbid medium based on the tree models
365 leaf area density ($m^2.m^{-3}$) and the aforementioned spherical leaf angle distribution
366 (LAD) (Figure 1b). Modelling the leaves as a turbid medium (Figure 1b), as opposed
367 to explicitly describing the 3D location, size and orientation of each scattering
368 element (Figure 1c), reduces the computational time required to simulate a scene
369 with 30% tree cover (173 trees) significantly (from 38 to 3 hrs on a 3.4Ghz quad-core
370 desktop CPU). Figure 3 shows that the 'through-canopy' FRP measure, expressed as
371 a percentage of that in the 'no canopy' situation, differs by in most cases less than 1%
372 and at the maximum 3.5% between the canopy described by discrete scattering
373 elements and that described as a turbid medium. Therefore, the turbid medium
374 canopy representation was used for all further experiments.

375 To determine percentage canopy cover, simulations were conducted for scenes
376 with no trees, and with an effectively opaque tree canopy developed by setting the
377 tree LAI of the turbid canopy to an extreme value (which, given the very low leaf
378 MWIR transmittance shown in Figure 1a, effectively prevents radiation transmission
379 through the grid cell). Cells containing vegetation were readily separable from non-
380 canopy cells, and these two contrasting simulations enabled percentage canopy cover
381 to be calculated at each sensor viewing direction.

382 Two approaches are taken to calculate total scene FRP for each simulation. In
383 the first, the opaque canopy simulations (where the tree LAI was set to an extreme
384 value) were used to identify the fire and non-fire surface cells observable at a given

viewing geometry, and these were respectively used to determine the background and fire radiance respectively (Equation 1). In the second, FRP in simulations where the canopy is described as a turbid medium was calculated by identifying all fire affected cells (e.g. those that are canopy obstructed and unobstructed) whose temperature is elevated above that of the 'background' surface temperature. The difference between these two approaches is that only the latter accounts for the transmission of MWIR radiation through the canopy.

Finally, to quantify the impact of vegetation interception on above-canopy FRP retrieval, 14 scenes were simulated where the percentage canopy cover was varied between 6 and 95%. Figure 4 illustrates the variation in apparent canopy cover with viewing geometry for canopies with a nadir canopy cover of (a) 6% and (b) 72%, calculated over the fire affected area itself (i.e. the 25m^2 area positioned centrally in the scene).

6. Results of simulating canopy effects on FRP retrieval

In DART, when converting 3D leaves to a turbid medium, the LAI can be user defined either relative to the total scene area or by the objects' vertical ground projection. In the simulations here, the latter approach is taken for defining canopy LAI, as this ensures the LAI of each tree is constant as the number of trees in the scene increases. This consequently results in the scene LAI increasing with increasing tree cover. For example, the LAI of scenes that have 6% canopy cover when viewed at nadir is 0.11, whilst that for scenes with 95% tree cover when viewed at nadir is 4.3.

For simulations conducted in a nadir-viewing situation, Figure 5 highlights the reduction in retrieved FRP as canopy cover increases, and compares the simulation-derived results from partly transmissive (e.g. turbid) and fully opaque

411 canopy situations. The turbid and opaque canopy models are described using the
412 same optical properties (Figure 1a) and canopy structural parameters (e.g. leaf,
413 branches and trunk), but the LAI of the opaque canopy is set sufficiently high so that
414 no energy is transmitted through the crowns, whereas the scene LAI of the turbid
415 canopy simulations increases from low values at low canopy covers (e.g. LAI = 0.1
416 and 6% canopy cover) to high values at high canopy covers (e.g. LAI = 4.3 at 95%
417 canopy cover).

418 For the opaque canopy case, retrieved FRP decreases linearly in response to
419 increasing canopy cover (Figure 5), and is simply a function of the area of fire
420 observed sensor. This agrees with the relationship found by Mathews *et al.* (2016) via
421 physical experimentation, denoted by the dotted line in Figure 5, and suggests that in
422 those experiments the vegetation density in areas covered by vegetation elements
423 was sufficiently high for the canopy to be effectively opaque. However, the turbid
424 media simulations of Figure 5 show a reduced level of FRP interception (by around
425 14%), due to the fact that's some fire emitted MWIR radiation is actually transmitted
426 through the canopy components.

427 Figure 6 explores the difference between opaque and partly transmissive
428 canopies further, showing the ratio of FRPs retrieved at the sensor in these two
429 situations and at a range of view angles as well as percentage canopy covers. As
430 percentage canopy cover increases, the ratio tends to zero since the turbid canopy
431 becomes increasingly dense and less transparent, and effectively acts to block the
432 FRP emitted by the fire in the same way as in the opaque canopy case. The opaque
433 trunks and branches reduce the retrieved FRP, and this is greatest at 95% canopy
434 cover where FRP is reduced by 11% at nadir and by ~50% at 68° view zenith relative
435 to the 'no canopy' simulation.

436

6.1 Canopy density (leaf area index)

To quantify the impact of canopy density, rather than canopy percentage cover, on retrieved FRP, tree LAI was varied between 0.25 and 4.0 in the simulations. Incrementing tree LAI rather than scene LAI ensures that all trees maintain the same vegetation structural characteristics, irrespective of canopy cover. For a tree LAI of 0.25, scene LAI was 0.005 (6% canopy cover), whilst for a tree LAI of 4.0 the scene LAI was 8.3 (95% canopy cover). Figure 7 highlights how nadir retrieved FRP emitted from surface fires is increasingly intercepted as overlying canopy cover increases. The relationship is well described by a 2nd order polynomial. Where canopy cover is <50% and LAI is < 1.0 less than 35% of the FRP is typically intercepted by the canopy. Once scene LAI exceeds unity and canopy cover is >70%, typically more than 45% of the FRP is intercepted, and the relationship starts to asymptote. Irrespective of canopy cover, for scene LAI >1.0 FRP is underestimated by ≥ 25%, and by >45% when the LAI exceeds 2.0.

Figure 8 illustrates the variation in sensor retrieved FRP as a function of view zenith angle and scene LAI for scenes of different percentage canopy covers. A reduction in retrieved FRP with view zenith angle is evident in all cases, and increases sharply with increasing canopy cover and scene LAI. At 6% canopy cover, the percentage of FRP intercepted at nadir and at 68.5° view zenith ranges from 0.8 to 3% and 5 to 16% with an LAI values of 0.01 and 0.21. At 95% canopy cover, the percentage of FRP intercepted at nadir and at 68.5° view zenith ranges is much greater; ranging between 32 - 60.5% at nadir (LAI 0.52) and between 92 - 99% at 68.5° view zenith (LAI 8.33). The latter represents an extreme case as active fire detections reduce significantly at large view zenith angles due to the larger pixel area (Freeborn *et al.*, 2011; Zhang *et al.*, 2017).

7.0 Physical Experiments in FRP canopy interception

To test our simulations, a series of small scale outdoor experiments were conducted to measure the impact of vegetation interception on FRP retrieval. Two AGEMA 550 thermal infrared cameras operating with a narrowband 3.9 μm MWIR filter very similar to that of MODIS Band 21 were used. The application of these cameras in FRP experiments has been described previously by Paugam *et al.* (2013) and Wooster *et al.* (2005). One camera was positioned at nadir 7 m above the fuel bed, and a second at the same distance but with a view zenith of 45° off-nadir. The fuel bed consisted of grass and pine needles evenly distributed across a 2 m × 2 m area. The two cameras were first used to measure the FRP during burns with no overlying canopy present, and a very strong linear relationship (r^2=0.99) seen between the two FRP retrievals. The off-nadir camera consistently recorded an FRP 12% lower than the nadir camera during the flaming (high FRP) period of the fire, caused by the differences in pixel area and heterogeneity of the fires 3D structure, and this upward adjustment was subsequently made to all the off-nadir camera's FRP retrievals in order to remove the angular dependence. The adjustment does not account for variations in FRP as a result of changing flame geometry over time, and therefore different path lengths through the flames, but it does provide a good bulk correction for the off-nadir FRE. Using a similar experimental design, Paugam *et al.* (2013) found differences between nadir and off-nadir FRE of 14 to 22% for fires where flaming activity was particularly strong, which reduced to 7 - 11% when flaming activity was less. In the experimental fires described here, flaming activity was present, which is evident at the start of the time series shown in Figure 9.

For the overlying canopy, freshly cut pine branches having live, green needles were positioned 4 m above the fuel bed, to create 53.5% vegetation cover when

488 viewed by the nadir camera, but still giving the off-nadir camera an uninterrupted
489 view. A fire with the same fuel type and load as previously described was conducted,
490 but now with the nadir camera viewing through the canopy. Active combustion
491 continued for around 10 minutes and Figure 9a presents the FRP data retrieved by
492 the nadir and off-nadir cameras, along with the ratio of the nadir to off-nadir FRP for
493 the period of active combustion (Figure 9b). The mean ratio between the canopy-
494 obscured and unobscured FRP retrievals is 0.49 (σ=0.057), meaning that the FRP is
495 underestimated by 51% due to the 53.5% vegetation cover. This is close to the level of
496 underestimation modelled in Figure 5, where FRP is underestimated by 54% when a
497 52.5% canopy cover was modelled using an opaque canopy element assumption.
498 When the tree crowns were modelled as a turbid medium however, the FRP
499 underestimation was less (38%) for the same canopy cover. In a further three
500 outdoor physical experiments with the same vegetation cover, the underestimation
501 remained relatively constant (54 - 58%), again in close agreement with the
502 simulations conducted using the opaque canopy assumption. Similar results were
503 found when the vegetation canopy cover was then increased to 60.1%, where during
504 three fires the thermal camera retrieved FRP was underestimated by 56% - 62%,
505 again far closer to that of the opaque canopy simulation (62% underestimation) than
506 the turbid medium simulation (44%).

507 An important distinction between the turbid canopy simulations and the
508 results of the physical experiment stems from the representation of the canopy leaf
509 material in the simulations. When the canopy is described as a turbid medium, the
510 vegetation density within each of the 0.25 cm^3 cells which cover the tree crown varies
511 widely, and many cells do not have sufficiently dense vegetation within them to
512 prevent the transmittance of MWIR radiation, despite the very low transmittance of
513 the individual leaves within this waveband (Figure 1a). Only when the percentage

514 canopy cover and LAI are very high do the transmittance characteristics of the turbid
515 cells approach those of an opaque canopy (Figure 6). In contrast, the opaque canopy
516 tree crown grid cells have very high leaf area densities, which largely controls MWIR
517 transmittance through the canopy. This setup better approximates the very high
518 spatial resolution MWIR thermal camera measurements made during the outdoor
519 experiments (7.8 mm pixels). At this very high spatial resolution and with the
520 vegetation sufficiently clumped, pixels in the thermal imagery are effectively opaque
521 at MWIR wavelengths, which is better simulated by DART when the canopy is
522 modelled as a collection of opaque objects. Overall, it is clear that differences exist
523 between the simulations able to be run using DART and the real situation
524 represented by the physical experiment, for example in vegetation structure, type,
525 and horizontal and vertical arrangement, as well as in the use of a uniform heat
526 source for the simulations as opposed varying temperatures in the real fire case.
527 However, modelling tree crowns as opaque does not accurately reflect the
528 transmittance characteristics of a real canopy, where there are varying leaf area
529 densities and attenuation profiles as you move through the canopy. Hence, our
530 simulations were conducted using the turbid medium assumption that better
531 represents this type of canopy characteristic.
532
533 **8.0 Significance for Satellite-derived FRP Measures**
534 Above canopy FRP retrievals can be adjusted for canopy interception using
535 the functions illustrated in Figures 7 and 8. This in theory enables satellite-derived
536 FRP retrievals to be adjusted for the impact of intervening tree canopies, and this
537 was investigated using the geostationary Meteosat SEVIRI FRP-PIXEL product
538 available from the EUMETSAT LSA SAF (Wooster *et al.*, 2015). This product is
539 available over Africa every 15 minutes at a 3 km spatial sampling distance at the sub-

satellite point, and we use the 2004-2012 time series here. Daily fire radiative energy (FRE) was calculated from these nine years of data by integrating the FRP values over the diurnal cycle at each pixel (Roberts and Wooster, 2014. To account for the influence of the overlying vegetation canopy and its associated LAI, the 8-day temporal resolution and 500m spatial resolution MODIS LAI product (MCD15A2H; Myneni *et al.*, 2002), was remapped to the SEVIRI measurement grid and used to calculate the mean LAI within each SEVIRI pixel. The percentage tree canopy cover for each SEVIRI pixel was similarly derived from the 1 km tree cover dataset (DeFries *et al.,* 2000).

To correct the FRE values for the effect of tree canopy interception we used the LAI value closest in time to each FRP observation. The relationship between FRP and canopy structure (LAI and canopy cover) is described by a 2nd order polynomial, where the model parameters vary with the LAI and canopy cover. The polynomial fits obtained between LAI and canopy cover at nadir are shown in Figure 7 which were similarly derived as a function of view zenith angle and illustrated in Figure 8. For each retrieved FRP, the polynomial applied to correct the SEVIRI FRP is that which is closest in value to the pixel LAI and percentage cover. All DART simulations conducted thus far assumed a MWIR spectral band representing that of MODIS Band 21 (3.929-3.989 μm). We made further simulations of the impact of 20% and 40% tree cover based on the Meteosat SEVIRI MWIR spectral band (nominal spectral range 3.44 - 4.36μm) instead of the MODIS spectral band, and these show differences of less than 1% between the SEVIRI and MODIS simulations. In general, SEVIRI retrieved slightly less FRP than MODIS (a mean of -0.38 % less at 20% tree cover and -0.87% less at 40% tree cover), but these are considered negligible for our work and primarily stem from

565 the greater spectral variability of the bark and soil optical properties across the
566 wider SEVIRI spectral range.

567 Figure 10a shows the annual estimated FRE for African fires, and the figure
568 once adjusted for canopy interception along with their percentage difference
569 (Figure 10b) which varies between 14 and 16.3% (mean of 15%). Marginally greater
570 interannual variation was present in the northern hemisphere (15.5% to 18.2%)
571 than in the southern hemisphere (17%-19.1%), and the impact of tree canopy cover
572 can be seen to be significant but cannot be responsible for the much larger
573 difference between the FRE to fuel consumption conversion factors derived from
574 spaceborne data (Kaiser *et al.*, 2012; Mota and Wooster, 2018) and small-scale
575 laboratory experiments on 'perfectly observed' fires (Wooster *et al.,* 2005)
576 identified in Section 1. The relatively modest impact of canopy cover on the overall
577 African FRE budget comes about because the vast majority (96%) of fire emitted
578 radiant energy occurs in areas with less than 40% tree cover, and with peak fire
579 activity confined to areas with only 10 to 20% tree cover (Figure 11). Areas with
580 more than 50% tree cover show minimal fire activity, likely a result of the high
581 relative humidity under such dense canopies (Cochrane, 2003), but perhaps also
582 because there is an increased probability of active fire detection omissions in such
583 situations (Freeborn *et al.*, 2014b). Spatially the greatest increase in FRE as a result
584 of the adjustment occurs in (southern hemisphere) northern Angola and southern
585 Democratic Republic of the Congo whilst northern Zambia, southern Angola and
586 central Mozambique, and (northern hemisphere) in southern Sudan, northern
587 Central Africa Republic, northern Ghana, southern Guinea and Sierra Leone. The
588 largest increase in FRE as a result of the correction for canopy cover and LAI is
589 found in Equatorial Guinea (32%) and Liberia (32%). However, the total FRE from
590 fires burning in these countries is low compared to other countries such as Angola

591 and Democratic Republic of Congo (DRC) where lower FRE increases of 17% and
592 22% respectively were found but which experience much greater levels of fire
593 activity.

594 Of course, simply adjusting sensor retrieved FRP in this way makes a number
595 of assumptions, such as that the tree cover is uniformly distributed within the pixel,
596 which maybe particularly unlikely in woodland transition zones. The approach also
597 assumes that all fires remain as surface burns and don't transition to crown fires,
598 though this is indeed rare in most of Africa (Trollope and Trollope, 2010). Finally,
599 the MODIS LAI data used to correct the FRP includes contributions from both the
600 tree and herbaceous layers although the latter is largely senescent and therefore
601 doesn't have a large LAI during the fire season. Kahui and Hanan (2017a) partitioned
602 MODIS LAI estimates over sub-Saharan Africa into woody and herbaceous LAI using
603 allometric relationships between canopy LAI and the dominant tree species. An
604 annual average (2003-2015) tree and herbaceous LAI dataset (Kahui and Hanan,
605 2017b) is available at an 8 day temporal resolution, and use of the tree LAI
606 component of this dataset in place of the basic MODIS LAI has very little impact on
607 the results (overall mean uplift in FRE due to the correction for canopy interception
608 increasing from the 15% of Figure 10b to 15.6%). The slightly higher adjustment
609 found when using the tree LAI dataset largely results from the gap filling and
610 temporal filtering applied to the MODIS LAI product in developing the tree LAI
611 dataset which can result in higher LAI estimates.

612

613 ## 9.0 Conclusion

614 This study has quantified the impact of overlying tree canopies on the retrieval
615 of fire radiative power (FRP) from surface vegetation fires for the first time. We have
616 used a 3D radiative transfer model to quantitatively demonstrate the impact of

canopy interception on above canopy (i.e. airborne or spaceborne) retrievals of FRP, and have confirmed with small scale experiments that FRP decreases in direct proportion to percentage vegetation cover as seen from the sensor viewing direction. Our 3D radiative transfer simulations using the DART model of Gastellu-Etchegorry, J-P. *et al.* (2015) show this same relationship when the vegetation canopy is modelled as opaque, but when represented as a turbid medium (which is generally more representative of real vegetation canopy situations), the degree of FRP interception occurring at any particular canopy cover decreases by around 14% compared to the opaque canopy case, and thus the level of FRP underestiamtion is itself underestimated. Analysis of the influence of scene LAI, through variation of the tree LAI metric, indicates nadir FRP is reduced by at least 20% when the LAI exceeds 1.0 and by >45% when the LAI is >2.0, irrespective of percentage tree cover.

The relationships found herein were used to adjust real geostationary FRE estimates made over Africa using the Meteosat SEVIRI sensor. Adjustments for the influence of tree canopy interception of the upwelling FRP were based on MODIS LAI and percentage tree cover products, and indicate that around 15% of surface fire emitted FRP is intercepted by tree canopies in Africa, with very little interannual variation (<2%). This assessment provides a route to adjust airborne and spaceborne FRP retrievals for the influence of canopy interception when developing fire emission inventories that incorporate FRP metrics, though other factors such as active fire detection errors of omission, and in particular the inability of active fire detection products to include the (often very numerous) low FRP fires must be responsible for the bulk of the significant regional-scale FRP underestimation seen with some FRP-based measures (e.g. Kaiser *et al.*, 2012; Mota and Wooster, 2018). Campaigns, such as the Prescribed Fire Combustion and Atmospheric Dynamics Research Experiment

642 (RxCADRE) and the Fire And Smoke Model Evaluation Experiment (FASMEE;
643 Ottmar *et al.*, 2017) will help elucidate further of these impacts.
644
645 ## 10.0 Acknowledgements
646 MODIS LAI and MODIS active fire data are distributed freely as part of NASA's
647 EarthData system (https://search.earthdata.nasa.gov/search). The SEVIRI FRP-
648 PIXEL data were provided by the EUMETSAT Land Surface Analysis Satellite
649 Application Facility (LSA SAF; https://landsaf.ipma.pt/). The MODIS derived tree
650 and herbaceous LAI dataset was downloaded from
651 http://datadryad.org/resource/doi:10.5061/dryad.v5s0j. The DART model was
652 provided freely by Paul Sabatier University (http://www.cesbio.ups-
653 tlse.fr/us/dart.html). We would like to thank the reviewers for their comments for
654 improving the manuscript. Funding for parts of this research was provided by NERC
655 grants (NE/M017958/1 and NE/M017729/1) and NERC's National Centre for Earth
656 Observation (NCEO).
657
658
659
660
661
662 ## 11.0 References
663 Andela, N., Kaiser, J. W., van der Werf, G. R., and Wooster, M. J. (2015) New fire
664 diurnal cycle characterizations to improve fire radiative energy assessments made
665 from MODIS observations. *Atmospheric Chemistry and Physics*. 15, 8831-8846.
666 doi:10.5194/acp-15-8831-2015
667

668 Andela, N., van der Werf, G. R., Kaiser, J. W., van Leeuwen, T. T., Wooster, M. J. and
669 Lehmann, C. E. R. (2016) Biomass burning fuel consumption dynamics in the tropics
670 and subtropics assessed from satellite. *Biogeosciences*. 13. 12, 3717-3734,
671 doi:10.5194/bg-13-3717-2016
672
673 Baldassarre, G., Pozzoli, L., Schmidt, C. C., Unal, A., Kindap, T., Menzel, W. P.,
674 Whitburn, S., Coheur, P.-F., Kavgaci, A., and Kaiser, J. W. (2015). Using SEVIRI fire
675 observations to drive smoke plumes in the CMAQ air quality model: a case study over
676 Antalya in 2008. *Atmospheric Chemistry and Physics*. 15. 14. 8539–8558.
677
678 Berk, A., Anderson, G.P., Acharya, P.K., Bernstein, L.S., Muratov, L., Lee, J., Fox, M.,
679 Adler-Golden, S.M., Chetwynd, J.H., Hoke, M.L., Lockwood, R.B., Gardner, J.A.,
680 Cooley, T.W., Borel, C.C., and Lewis, P.E. (2005). MODTRAN (TM) 5, a reformulated
681 atmospheric band model with auxiliary species and practical multiple scattering
682 options: Update. *Algorithms and Technologies for Multispectral, Hyperspectral,*
683 *and Ultraspectral Imagery XI, 5806*, 662-667
684
685 Boschetti, L. and Roy, D. P. (2009) Strategies for the fusion of fire radiative power
686 with burned area data for fire radiative energy derivations. *Journal of Geophysical*
687 *Research*. 114. D20302. doi:10.1029/2008JD011645.
688
689 Boyd, D. S. and Petitcolin, F. (2004) Remote sensing of the terrestrial environment
690 using middle infrared radiation (3.0-5.0μm). *International Journal of Remote*
691 *Sensing*. 25. 17. 3343-3368. doi: 10.1080/01431160310001654356
692

693 Calle, A., Casanova, J-L. and Gonzales-Alonso, F. (2009) Impact of point spread
694 function of MSG SEVIRI on active fire detections. *International Journal of Remote*
695 *Sensing*. 30. 17. 4567-4579.
696
697 Chuvieco, E., Yue, C., Heil, A., Mouillot, F., Alonso-Cana, I., Padilla, M., Pereira, J.
698 M., Oom, D., and Tansey, K. (2016) A new global burned area product for climate
699 assessment of fire impacts. *Global Ecology and Bioogeography*. 25. 5. 619-629.
700
701 Chuvieco, E., Riano, D., Danson, F. M., and Martin, P. (2006) Use of a radiative
702 transfer model to simulate the post-fire spectral response to burn severity. *Journal*
703 *of Geophysical Research*. 111. GS04S09. Doi:10.1029/2005JG000143.
704
705 Cochrane, M. A., Fire science for rainforests. *Nature*. 421.913-919.
706
707 DeFries, R., M. Hansen, J.R.G. Townshend, A.C. Janetos and T.R. Loveland (2000) A
708 new global 1km data set of percent tree cover derived from remote sensing. *Global*
709 *Change Biology*. 6. 247-254.
710
711 Dennison, P. E., Charoensiri, K., Roberts, D. A., Peterson, S. H., Green, R., O. (2006)
712 Wildfire temperature and land cover modeling using hyperspectral data. *Remote*
713 *Sensing of Environment*. 100. 212-222. doi:10.1016/j.rse.2005.10.007
714

715 Disney, M. I., Lewis, P., Gomez-Dans, J., Roy, D., Wooster, M. J., and Lajas, D.
716 (2011) 3D radiative transfer modelling of fire impacts on a two-layer savanna system.
717 *Remote Sensing of Environment*. 115. 1866-1881.
718
719 Ellicott, E., Vermote, E., Giglio, L., and Roberts, G (2009) Estimating biomass
720 consumed from fire using MODIS FRE. *Geophysical Research Letters*. 36. L13401,
721 doi:10.1029/2009GL038581.
722
723 Freeborn, P. H., Wooster, M. J., Hao, W. M., Ryan, C. A., Nordgren, B. L, Baker, S. P.
724 and Ichoku, C. (2008) Relationships between energy release, fuel mass loss, and
725 trace gas and aerosol emissions during laboratory biomass fires. *Journal of*
726 *Geophysical Research*. 113. D01301. doi:10.1029/2007JD008679
727
728 Freeborn, P.H., Wooster, M.J., Roberts, G., Malamud, B.D., & Xu, W.D. (2009).
729 Development of a virtual active fire product for Africa through a synthesis of
730 geostationary and polar orbiting satellite data. *Remote Sensing of Environment, 113*,
731 1700-1711
732
733 Freeborn, P.H., Wooster, M.J., & Roberts, G. (2011). Addressing the spatiotemporal
734 sampling design of MODIS to provide estimates of the fire radiative energy emitted
735 from Africa. *Remote Sensing of Environment, 115*, 475-489.
736
737 Freeborn, P. H., Wooster, M. J., Roy, D. P., and Cochrane, M. A. (2014a)
738 Quantification of MODIS fire radiative power (FRP) measurement uncertainty for
739 use in satellite-active fire characterisation and biomass burning estimation.
740 *Geophysical Research Letters*. 41. 6. 1988-1994.

741

742 Freeborn, P. H., Wooster, M. J., Roberts, G. and Xu, W. (2014b) Evaluating the
743 SEVIRI Fire Thermal Anomaly Detection Algorithm across the Central African
744 Republic Using the MODIS Active Fire Product. *Remote Sensing*. 6. 1890-1917.
745 Doi:10.3390/rs6031890.

746

747 Gastellu-Etchegorry, J. P., Demarez, V., Pinel, V. and agolski, F. (1996) Modelling
748 radiative transfer in heterogeneous 3-D vegetation canopies. *Remote Sensing of*
749 *Environment*. 58. 131-156.

750

751 Gastellu-Etchegorry, J-P., Yin, T., Lauret, N., Cajgfinger, T., Gregoire, T., Grau, E.,
752 Feret, J-B., Lopes, M., Guilleux, J., Dedieu, G., Malenovsky, Z., Cook, B. D., Morton,
753 D., Rubio, J., Durrieu, S., Cazanave, G., Martin, E. Ristocelli, T. (2015) Discrete
754 Radiative Transfer (DART 5) for modelling airbone and satellite spectrometer and
755 LiDAR acquisitions of natural and urban landscapes. *Remote Sensing*. 7. 2. 1667-
756 1701. Doi:10.3390/rs70201667.

757

758 Giglio, L. Randerson, J. T. and van der Werf, G. R. Kasibhatla (2013) Analysis of
759 daily, monthly and annual burned area using the fourth-generation global fire
760 emissions database (GFED4). *Journal of Geophysical Research : Biogeosciences*.
761 118. 1. 317-328.

762

763 Grau, E. and Gastellu-Etchegorry, J. P. (2013) Radiative transfer modelling in the
764 Earth-Atmosphere system with DART model. *Remote Sensing of Environment*. 130.
765 149-170.

766

767 Grigal, O. F. and Ohmann, L. F. (1992) Carbon storage in upland forests of the lake
768 states. *Soil Science Society of America Journal*. 56: 935-943.

769

770 Guillevic, P., Gastellu-Etchegorry, J. P., Demarty, J. and Prevot, L (2003) Thermal
771 infrared radiative transfer within three-dimensional vegetation covers. *Journal of*
772 *Geophysical Research*. 108. D8. Doi:10.1029/2002JD002247.

773

774 Ichoku, C. and Kaufman, Y.J. (2005). A method to derive smoke emission rates
775 from MODIS fire radiative energy measurements. *IEEE transactions on Geoscience*
776 *and Remote Sensing*. 43. 11. 2636-2649.

777

778 Ito, A. and Penner, J. E. (2004) Global estimates of biomass burning emissions based
779 on satellite imagery for the year 2000. *Journal of Geophysical Research*. 109.
780 D14S05. Doi:10.1029/2003JD004423.

781

782 Jenkins, B. M., Baxter, L. L., Miles Jr, T. R., and Miles, T. R. (1998) Combustion
783 properties of biomass. *Fuel Processing Technology*. 54. 17 – 46

784

785 Johnson, E. D. (1992) Fire and Vegetation Dynamics: Studies from the North
786 American Boreal Forest. *Cambridge University Press*. Cambridge.

787

788 Johnston, J.M., Wooster, M. J., and Lynham, T. J. (2014) Experimental
789 confirmation of the MWIR and LWIR grey body assumption for vegetation fire
790 flame emissivity. *International Journal of Wildland Fire*. 23. 4. 463-479.

791

792 Kahiu, M. N. and Hanan, N. P. (2017a) Estimation of woody and herbaceous leaf are
793 index in sub-Saharan Africa using MODIS data. *Journal of Geophysical Research :*
794 *Biogeosciences*. 122. Doi:10/1002/2017JG004105
795
796 Kahiu M. N and Hanan, N. P. (2017b) Data from: Estimation of woody and
797 herbaceous leaf area index in Sub-Saharan Africa using MODIS data. *Dryad Digital*
798 *Repository*. https://doi.org/10.5061/dryad.v5s0j
799
800 Kaiser. J. W., Heil, A., Andrae, M. O., Benedettie, A., Chubarova, N., Jones, L.,
801 Morcrette, J-J., Razinger, M., Schultz, M. G., Suttie, M. and van der Werf, G., R.
802 (2012) Biomass burning emissions estimates with a global fire assimilation system
803 based on observed fire radiative power. *Biogeosciences*. 9. 5125-5142.
804 doi:10.5194/bg-9-5125-2012
805
806 Kallel, A. and Gastellu-Etchegorry, J. P. (2017) Canopy polarized BRDF simulation
807 based on non-stationary Monte Carlo 3-D vector RT modelling. *Journal of*
808 *Quantitative Spectroscopy and Radiative Transfer*. 189. 149-167.
809
810 Kaufman, Y. J., Justice, C. O., Flynn, L. P., Kendall, J. D., Prins, E. M., Giglio, L.,
811 Ward, D. E., Menzel, P., Setzer, A. W. (1998) Potential global fire monitoring from
812 EOS-MODIS. *Journal of Geophysical Research*. 103. D24. 32215-32238.
813
814 Kaufman, Y. J., Remer, L., Ottmar, R., Ward, D., Rong-R, L., Kleidman, R., Frase, R.,
815 Flynn, L., McDougal, D., and Shelton, G. (1996) Relationship between remotely
816 sensed fire intensity and rate of emission of smoke : SCAR-C experiment. In J,
817 Levine (Ed.), Global biomass burning (pp. 685 – 696). MA: MIT Press.

Kaufman Y., L. Remer, R. Ottmar, D. Ward, L. Rong-R, R. Kleidman, R. Fraser, L. Flynn, D. McDougal, and G. Shelton (1996) Relationship between remotely sensed fire intensity and rate of emission of smoke: SCAR-C experiment, in *Global Biomass Burning*, Levine, J. (ed), 685-696, MIT Press, Mass.

Kremens, R.L., Dickinson, M.B., & Bova, A.S. (2012). Radiant flux density, energy density and fuel consumption in mixed-oak forest surface fires. *International Journal of Wildland Fire, 21*, 722-730

Laguarde, J-P., Henon, A., Kurz, B., Moreau, P, Irvine, M, Voogt, J. and Mestayer, P. (2010) Modelling daytime thermal directional anisotropy over Toulouse city centre. Remote Sensing of Environment. 114. 87-105. doi:10.1016/j.rse.2009.08.012

Laguarde, J-P., Henon, A., Irvine, M., Voogt, J., Pigeon, G., Moreau, P., Masson, V., and Mestayer, P. (2012) Experimental characterisation and modelling of the nighttime directional anisotropy of thermal infrared measurements over an urban area : Case study of Toulouse (France). *Remote Sensing of Environment*. 117. 19-33. doi:10.1016/j.rse.2011.06.022

Li, F., Zhang, X., Kondragunta, S., Roy, D.P., 2018, Investigation of the fire radiative energy biomass combustion coefficient: A comparison of polar and geostationary satellite retrievals over the Conterminous United States. *Journal of Geophysical Research: Biogeosciences*, 123, 722–739.

843 Mathews, B.J., Strand, E.K., Smith, A.M., Hudak, 846 A.T., Dickinson, B. &
844 Kremens, R.L. (2016). Laboratory experiments to estimate interception of infrared
845 radiation by tree canopies. *International Journal of Wildland Fire*. 25. 9. pp.1009-
846 1014.
847
848 Malenovsky, Z., Martin, E., Homolova, L., Gastellu-Etchgorry, J-P., Zurita-Milla, R.,
849 Schaepman, M. E., Pokorny, R., Clevers, J. G. P. W., and Cudlin, P. (2008) Influence
850 of woody elements of a Norway spruce canopy on nadir reflectance simulated by the
851 DART model at very high spatial resolution. *Remote Sensing of Environment*. 112. 1-
852 18.
853
854 Morton, D. D. C., Rubio, J., Cook, B. D., Gastellu-Etchegorry, J-P., Longo, M., Choi,
855 H., Hunter, M., and Keller, M. (2016) Amazon forest structure generates diurnal
856 and seasonal variability in light utilization. *Biogeosciences* 13. 2195-2206.
857
858 Morton, D. C., DeFries, R. S., Nagol, J., Souza Jr, C. M., Kasischke, E. S., Hurtt, G. C.,
859 and Dubayah, R. (2011) Mapping canopy damage from understory fires in Amazon
860 forests using annual time series of Landsat and MODIS data. *Remote Sensing of*
861 *Environment*. 115. 1706-1720.
862
863 Mota, B. and Wooster, M. J. (2018) A new top-down approach for directly estimating
864 biomass burning emissions and fuel consumption rates and totals from geostationary
865 satellite fire radiative power (FRP). *Remote Sensing of Environment*. 206. 45-62.
866 Doi:10.1016/j.rse.2017.12.016.
867

868 Mu, M., Randerson, J. T., van der Werf, G. R., Giglio, G., Kasibhatla, P., Morton, D.,
869 Collatz, G. J., DeFries, R. S., Hyer, E. J., Prins, E. M., Griffith, D. W. T., Wunch, D.
870 Toon, G. C., Sherlock, V., Wennberg, P. O. (2011) Daily and 3-hourly variability in
871 global fire emissions and consequences for atmospheric model predictions of carbon
872 monoxide. *Journal of Geophysical Research : Atmospheres*. 116. D24. Doi:
873 10.1029/2011JD016245
874
875 Myneni, R.B., Smith, G.R., Lotsch, A., Friedl, M., Morisette, J.T., Votava, P.,
876 Running, S.W., Hoffman, S., Knyazikhin, Y., Privette, J.L., Glassy, J., Tian, Y., Wang,
877 Y., Song, X., Zhang, Y., Smith, G. R., Lotsch, A., Friedl, M., Morisette, J. T., Votava,
878 P., Nemani, R. R., and Running, S. W., (2002) Global products of vegetation leaf area
879 and fraction absorbed PAR from year one of MODIS data. *Remote Sensing of*
880 *Environment*. 83. 214–231.
881
882 Nilson, T. (1971) A theoretical analysis of the frequency of gaps in plant stands.
883 *Agricultural Meteorology*. 8. C. 25-38.
884
885 Ottmar R, Brown, T. J., French, N. H. F. and Larkin, N. K. (2017). Fire and Smoke
886 Model Evaluation Experiment (FASMEE) study plan. *Joint Fire Sciences Program*
887 *Project* 15-S-01-01, 148 pp
888
889 Parent, G., Acem, Z., Lechene, S., and Boulet, P. (2010) Measurement of infrared
890 radiation emitted by the flame of a vegetation fire. *International Journal of Thermal*
891 *Science*s. 49. 555-562.
892

893 Pereira, J. M. C., (1999) A comparative evaluation of NOA/AVHRR vegetation
894 indexes for burned surface detection and mapping. *IEEE Transactions on*
895 *Geosciences and Remote Sensing*. 37. 1 . 217-226. DOI: 10.1109/36.739156
896
897 Pereira, J. M. C., Mota, B., Privette, J. L., Caylor, K. K., Silva, J., M. N., Sa, A. C. L.
898 and Ni-Meister, W. (2004) A simulation analysis of the detectability of understory
899 burns in Miombo woodlands. *Remote Sensing of Environment*. 93. 296-310.
900
901 Pereira, G., Freitas, S. R., Moraes, E. C., Ferreira, N. J., Shimabukuro, Y. E.,
902 Brahmananda, V. Longo, K. M. (2009) Estimating trace gas and aerosol emissions
903 over South America : Relationship between fire radiative energy released and aerosol
904 optical depth observations. *Atmospheric Environment*. 43. 40. 6388-6397.
905
906 Pereira, G., Shimabukuro, Y. E., Moraes, E. C., Freitas, S. R., Cardozo, F., S., and
907 Longo, K. M. (2011) Monitoring the transport of biomass burning emission in South
908 America. *Atmospheric Pollution Research*. 3. 247-254.
909
910 Paugam, R, Wooster, M. J., and Roberts, G. (2013) Use of handheld thermal imager
911 data for airborne mapping of Fire Radiative Power and energy and flame front rate of
912 spread. *IEEE Transactions on Geoscience and Remote Sensing*. 99. 1-15. doi:
913 10.1109/TGRS.2012.2220368
914
915 Pisek, J. Sonnentag, O., Richardson, A. D. and Mottus, M. (2013) Is the spherical leaf
916 inclination angle distribution a valid assumption for temperate and boreal broadleaf
917 species? *Agricultural and Forest Meteorology*. 169. 186-194.

Stott, P. (2000) Combustion in tropical biomass fires : a critical review. *Progress in Physical Geography*. 24. 3. 355-377

Randerson, J.T., Chen, Y., Werf, G.R., Rogers, B.M. & Morton, D.C. (2012). Global burned area and biomass burning emissions from small fires. *Journal of Geophysical Research: Biogeosciences*. 117. G4. doi:doi.org/10.1029/2012JG002128

Roberts, G. and Wooster. M., J. (2008) Fire Detection and Fire Characterization over Africa using Meteosat SEVIRI. *IEEE Transactions on Geoscience and Remote Sensing*. 48. 4. 1200-1219

Roberts, G., Wooster, M. J., Freeborn, P. H. and Xu, W. (2011) Integration of geostationary FRP and polar-orbiting burned area datasets for an enhanced emissions inventory. *Remote Sensing of Environment*. 115. 2047-2061. doi:10.1016/j.rse.2011.04.006

Roberts, G., Wooster, M. J., Xu, W., Freeborn, P. H., Morcrette, J-J., Jones, L., Benedetti, A. and Kaiser, J. (2015) LSA SAF Meteosat FRP Products : Part 2 – Evaluation and demonstration of use in the Copernicus Atmosphere Monitoring Service (CAMS). *Atmospheric Chemistry and Physics*. 15. 13241-13267.

Robinson, J. M., (1991) Fire from space: global fire evaluation using infrared remote sensing. *International Journal of Remote Sensing*. 12. 3-24.

944

945 Ross, J. (1981) The radiation regime and architecture of plant stands. The Hague : Dr
946 Junk Publishers.

947

948 Salisbury, J. W. and D'Aria, D. M. (1994) Emissivity of terrestrial materials in the 3-5
949 μm atmospheric window. *Remote Sensing of Environment*. 47. 345-361.

950

951 Schneider, F. D., Leiterer, R., Morsdorf, F., Gastellu,-Etchegorry, J-P., Lauret, N.,
952 Pfeifer, N., and Schaepman, M. E. (2014) Simulating imaging spectrometer data : 3D
953 forest modelling based on LiDAR and in situ data. *Remote Sensing of Environment*.
954 152. 235-250.

955

956 Schroeder, W., Ellicott, E., Ichoku, C., Ellison, L., Dickinson, M. B., Ottmar, R. D.,
957 Clements, C., Hall, D., Ambrosia, V., Kremens, R. (2014) Integrated active fire
958 retrievals and biomass burning emissions using complementary near-coincident
959 ground, airborne and spaceborne sensor data. *Remote Sensing of Environment*. 140.
960 719-730. Doi: dx.doi.org/10.1016/j.rse.2013.10.010

961

962 Sepulcre-Canto, G., Zarco-Tejeda, P. J., Sobrino, J. A., Berni, J. A. J., Jiminenez-
963 Munoz, J. C., Gastellu-Etchegorry, J. P. (2009) Discriminating irrigated and rainfed
964 olive orchards with thermal ASTER imagery and DART 3D simulation. *Agricultural*
965 *and Forest Meteorology*. 149. 962-975. doi:10.1016/j.agriformet.2008.12.001.

966

967 Smith, A.M.S., Tinkham, W.T., Roy, D.P., Boschetti, L., Kremens, R.L., Kumar, S.S.,
968 Sparks, A. and Falkowski, M.J. (2013) Quantification of fuel moisture effects on

969 biomass consumed derived from fire radiative energy retrievals. *Geophysical*
970 *Research Letters*. 40. 1-5. doi:10.1002/2013GL058232
971
972 Sobrino, J. A., Mattar, C., Gastellu-Etchegorry, J-P., Jimenez-Munoz, J. C. and Grau,
973 E. (2011) Evaluation of the DART 3D model in the thermal domain using
974 satellite/airborne imagery and ground-based measurements. *International Journal*
975 *of Remote Sensing*. 32. 22. 7453-7477. Doi:10.1080/01431161.2010.524672
976
977 Trollope, W., S., W and Trollope, L. A., (2010) Fire effects and management in
978 African grasslands and savannas. In Squires, V. R., (Ed) Range and animal sciences
979 and resources management. Volume II. Encyclopedia of life support systems. Eolss
980 Publisgers Co. Ltd. United Kingdon. Pp 121-146.
981
982 van der Werf, G. R., Randerson, J. T., Collatz, G. J., and Giglio, L. (2003) Carbon
983 emissions from fires in tropical and subtropical ecosystems. *Global Change Biology*.
984 9. 4. 547 – 562.
985
986 van der Werf, G. R., Randerson, J. T., Giglio, L., Collatz, G. J., Mu, M., Kasibhatla, P.
987 S., Morton, D. C., DeFries, R. S., Jin, Y. and van Leeuwen, T. T. (2010) Global fire
988 emissions and the contribution of deforestation, savanna, forest, agricultural, and
989 peat fires (1997-2009). *Atmospheric Chemistry and Physics*. 10. 11707-11735.
990
991 van Leeuwen, T. T., der Werf, G. R., Hoffmann, A. A., Detmers, R. G., Rucker, G.,
992 French, N. H. F., Archibald, S., Carvalho Jr., J. A., Cook, G. D., de Groot, W. J.,
993 Hely, C., Kasischke, E. S., Kloster, S., McCarty, J. L., Pettinari, M. L., Savadogo, P.,
994 Alvarado, E. C., Boschetti, L., Manuri, S., Meyer, C. P., Siegert, F., Trollope, L. A. and

995 Trollope, W. S. W (2014) Biomass burning fuel consumption rates: a field
996 measurement database. *Biogeosciences*. 11.24. 7305-7329.doi:10.5194/bg-11-7305-
997 2014
998
999 Vermote, E., Ellicott, E., Dubovik, O., Lapyonok, T., Chin, M., Giglio, L. and Roberts,
1000 G. (2009) An approach to estimate global biomass burning emissions of Organic and
1001 Black Carbon from MODIS Fire Radiative Power. *Journal of Geophysical Research*.
1002 114. D18205. doi:10.1029/2008JD011188.
1003
1004 Widlowski, J.-L., Taberner, M., Pinty, B., Bruniquel-Pinel, V., Disney, M., Fernandes,
1005 R., Gastellu-Etchegorry, J-P., Gobron, N., Kuusk, A., Lavergne, P., Leblamc, S.,
1006 Lewis, P. E., Martin, E., Mottus, M., North, P. R. J., Qin, W., Robustelli, M., Rochdi,
1007 N., Ruiloba, R., Soler, C., Thompson, R., Verhoef, W., Verstraete, M. M. and Xie, D.
1008 (2007) Third radiation transfer model intercomparison (RAMI) exercise :
1009 Documenting progress in canopy reflectance models. *Journal of Geophysical*
1010 *Research*. 112. D09111. Doi:10.1029/2006JD007821
1011
1012 Widlowski, J-L., Robustelli, M., Disney, M., Gastellu-Etchegorry, J-P.,Lavergne, P.,
1013 Lewis, P., North, P. R. J., Pinty, B., Thompson, R. and Verstraete, M. M. (2008) The
1014 RAMI On-line Model Checker (ROMC) : A web-based benchmarking facility for
1015 canopy reflectance models. Remote Sensing of Environment. 112. 3. 1144-1150.
1016
1017 Widlowski, J-L., Pinty, B., Lopatka, M., Atzberger, C., Buzica, D., Chelle, M., Disney,
1018 M., Gastellu-Etchegorry, J-P., Gerboles, M., Gobron, N., Grau, E., Huang, H., Kallel,
1019 A., Kobayashi, H., Lewis, P. E., Qin, W., Schlerf, M., Struckens, J., Xie, D. (2013) The
1020 fourth radiation transfer model intercomparison (RAMI-IV) : Proficiency testing of

canopy reflectance models with ISO-13528. *Journal of Geophysical Research : Atmospheres*. 118. 13. 6869-6890

Wooster, M.J., Zhukov, B. and Oertel, D. (2003) Fire radiative energy for quantitative study of biomass burning: Derivation from the BIRD experimental satellite and comparison to MODIS fire products, *Remote Sensing of Environment*, 86, 83-107

Wooster, M. J., Roberts, G., Perry, G. L. W. and Kaufman, Y. J. (2005) Retrieval of biomass combustion rates and totals from fire radiative power observations: FRP derivation and calibration relationships between biomass consumption and fire radiative energy release. *Journal of Geophysical Research*. 110, D24311. doi:10.1029/2005JD006318

Wooster, M. J., Roberts, G., Freeborn, P. H., Xu, W., Govaerts, Y., Beeby, R., He, J., Lattanzio, A. and Mullen, R. (2015) Meteosat SEVIRI Fire Radiative Power (FRP) products from the Land Surface Analysis Satellite Applications Facility (LSA SAF) – Part 1 : Algorithms, product contents and analysis. *Atmospheric Chemistry and Physics*. 15. 9815-9895.

Xu, W., Wooster, M. J., Roberts, G., and Freeborn, P. (2010) New GOES imager algorithms for cloud and active fire detection and fire radiative power assessment across North, South and Central America. *Remote Sensing of Environment*. 114. 9. 1876-1865. https://doi.org/10.1016/j.rse.2010.03.012

Yin, Y., Cais, P., Chevallier, F., van der Werf, G. R., Fanin, T., Broquet, G., Boesch, H., Cozic, A., Hauglustaine, D., Szopa, S. And Wang, Y. (2016) Variability of fire carbon emissions in equatorial Asia and its nonlinear sensitivity to El Nino. Geophysical Research Letters. 43. 19. 10472-10479. Doi: 10.1002/2016GL070971

Zhang, X., Kondragunta, S., Ram, J., Schmidt, C. and Hung, H-C. (2012) Near-real-time global biomass burning emissions product from geostationary satellite constellation. *Journal of Geophysical Research : Atmospheres*. 117. doi:10.1029/2012JD017459.

Zhang., T., Wooster, M. J., and Xu, W. (2017) Approaches for synergistically exploiting VIIRS I- and M-Band data in regional active fire detection and FRPO assessment : A demonstration with respect to agricultural residue burning in Eastern China. *Remote Sensing of Environment*. 198. 407-424. Doi: 10.1016/j.rse.2017.06.028

Zhukov, B., Lorenz, E., Oertel, D., Wooster, M. and Roberts, G. (2006) Spaceborne detection and characterisation of fires during the bi-spectral infrared detection (BIRD) experimental small satellite mission (2001-2004). *Remote Sensing of Environment*. 100. 29-51. doi:10.1016/j.rse.2005.09.019

Zhukov, B., Lorenz, E., Oertel, D., Wooster, M., & Roberts, G. (2005). Spaceborne detection and characterization of fires during the bi-spectral infrared detection (BIRD) experimental small satellite mission. *DLR-Forschungsberich*. 96pp

Scene Parameters	**Parameter Value**
Scene Area	50m x 50m
Cell Dimensions	0.25m x 0.25m x 0.25m
Surface Temperature	310 K
Fire Area	25m x 25m
Fire Temperature	1000 K
Viewing Geometry	0-80° (view zenith), 0-360° (view azimuth)
Solar Geometry	30° (solar zenith), 225° (solar azimuth)
Spectral Range	3.929-3.989 μm
Vegetation Parameters	
Tree Dimensions	2.3m (length) x 2.3m (width) x 2.8m (height)
Leaf Angle Distribution	Spherical
Leaf Temperature	300 K
Trunk & Branch Temperature	295 K
Tree Leaf Area Index (LAI)	0.1 – 4.0 $m^2.m^{-2}$
Canopy Percentage Cover	6% - 95%
Number of trees per scene	25 - 948
Tree LAI	0.25 – 4.0 $m^2.m^{-2}$
Scene LAI	0.005 – 8.3 $m^2.m^{-2}$

Table 1 : Structural parameter values used to describe scenes and objects in the DART simulations

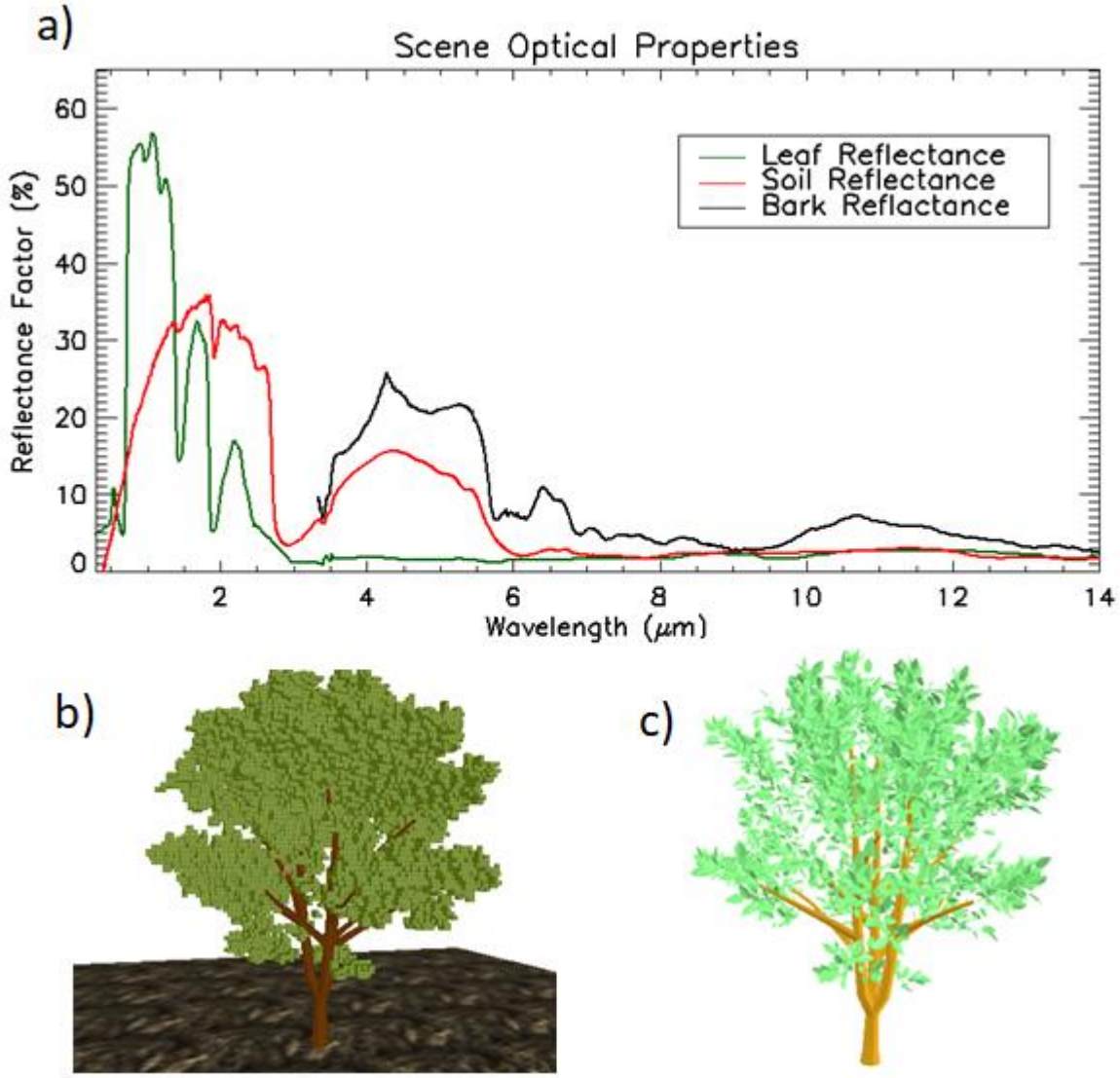

Figure 1: DART simulation information. (a) Spectral reflectance of leaf, bark and soil materials used within the simulations, (b) turbid representation of the tree object composed of discrete elements consisting of discrete scattering elements (c) at 3cm spatial resolution and where branches are represented as triangles and vegetation as a turbid medium.

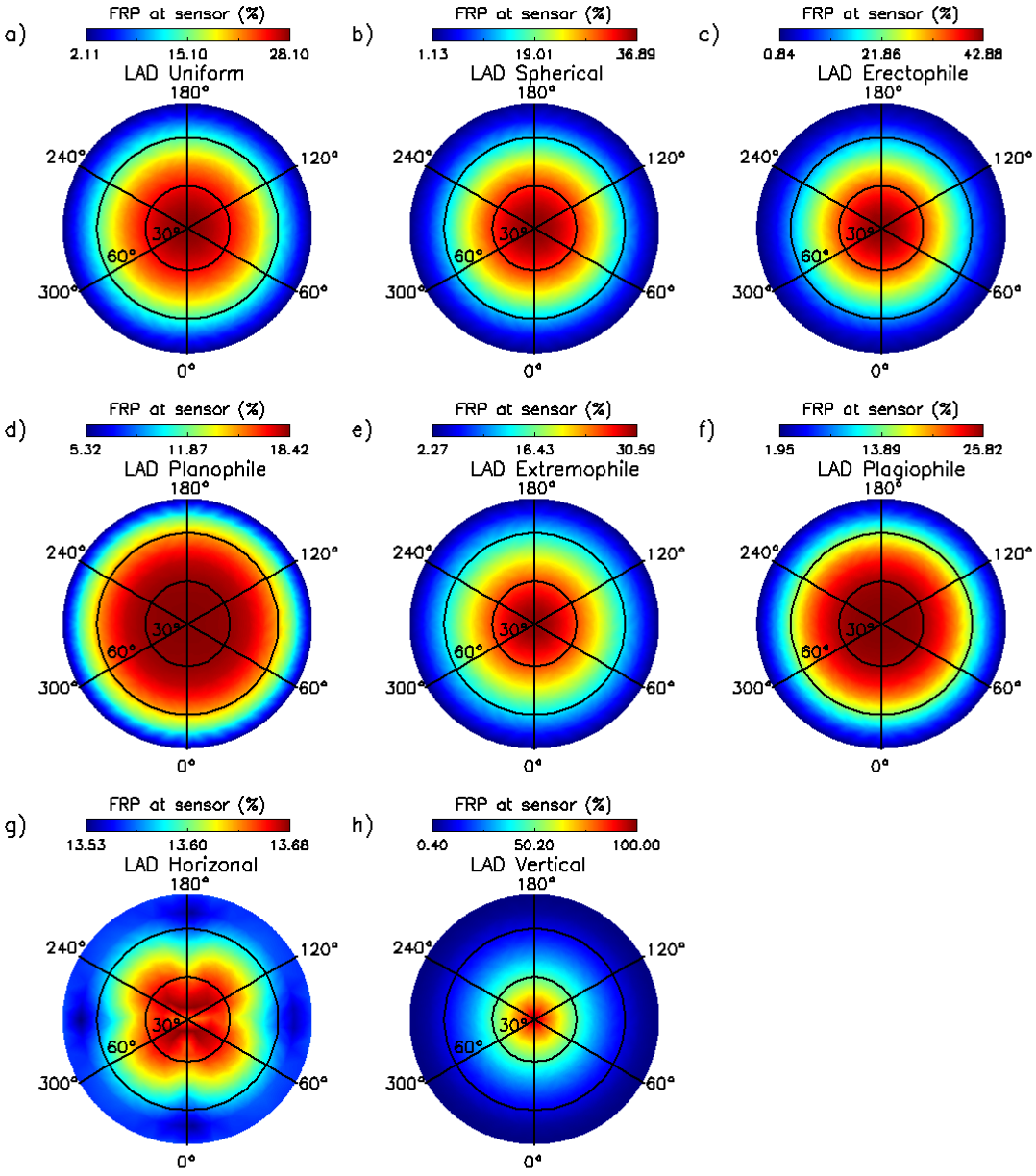

Figure 2: The amount of surface fire FRP retrieved when viewing through an overlying tree canopy, expressed as a percentage of the 'no-canopy' FRP value made from the same sensor observing from the same viewing direction. Each polar plot represents a canopy described using one of eight leaf angle distributions (LADs). In these polar plots, the view azimuth angle (0-360°) is indicated by the azimuth axis whilst the view zenith angle (0-80°) is described by the polar axis.

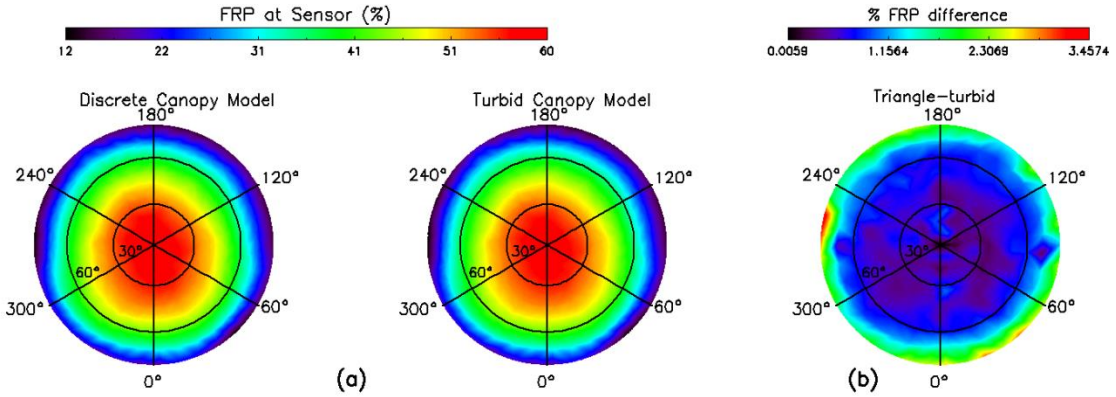

Figure 3: The amount of surface fire FRP retrieved when viewing through an overlying tree canopy, expressed as a percentage of the 'no-canopy' FRP value made from the same sensor observing from the same viewing direction. Here the canopy cover over the fire is 30% when observed from nadir, and the simulations were conducted using (a) both discrete element simulations based on tree canopy representations of the type shown in Figure 1c, and turbid media canopy simulations of the type shown in Figure 1b. (b) Differences in the results obtained with these simulations is small (<4%). In these polar plots, the view azimuth angle (0-360°) is indicated by the azimuth axis whilst the view zenith angle (0-80°) is described by the polar axis.

a) b)

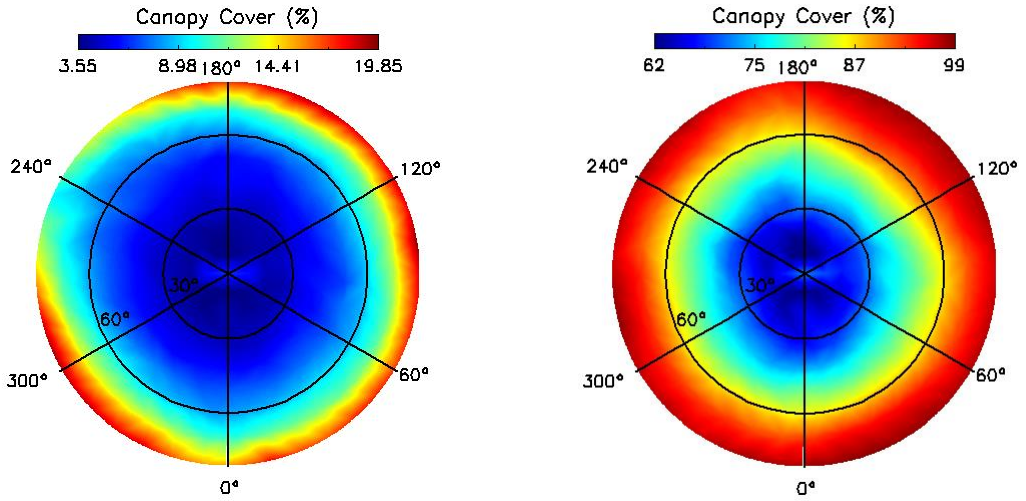

Figure 4: Angular variation in percentage canopy cover with viewing geometry for scenes simulated with (a) 6% and (b) 72% tree cover at nadir over the active fire area. Canopy cover is not symmetric as the trees are randomly distributed around the scene. A spherical leaf angle distribution was assumed.

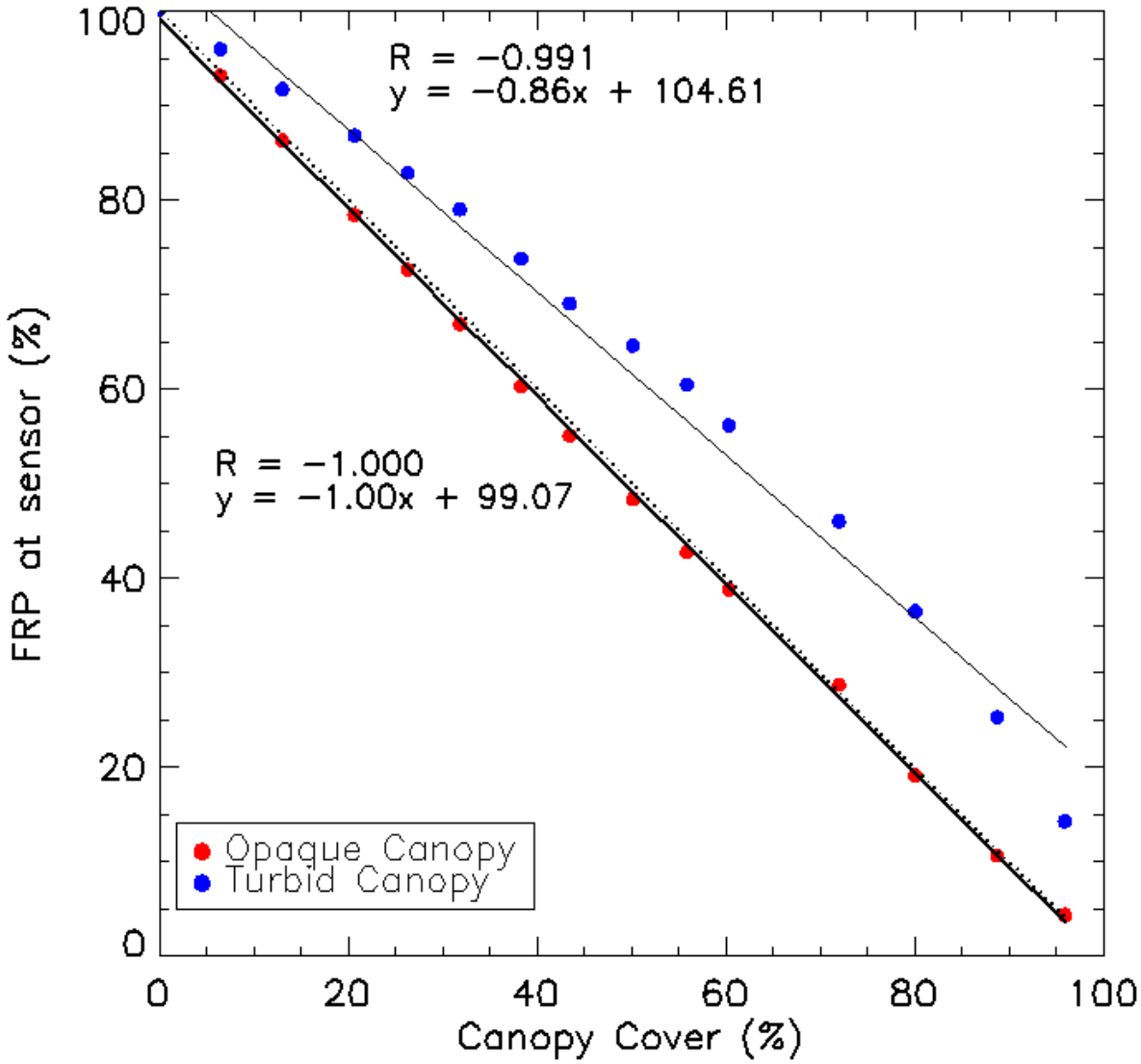

Figure 5: The impact of retrieving FRP through a vegetation canopy modelled as both an opaque and turbid media. FRP retrieved though the canopy is expressed as a percentage of that retrieved in the 'no canopy' situation by the same sensor observing with the same viewing geometry (here assumed to be nadir in both cases). Also shown (dotted line) is relationship found by Mathews *et al.* (2016), which is nearly identical to the opaque canopy situation modelled herein.

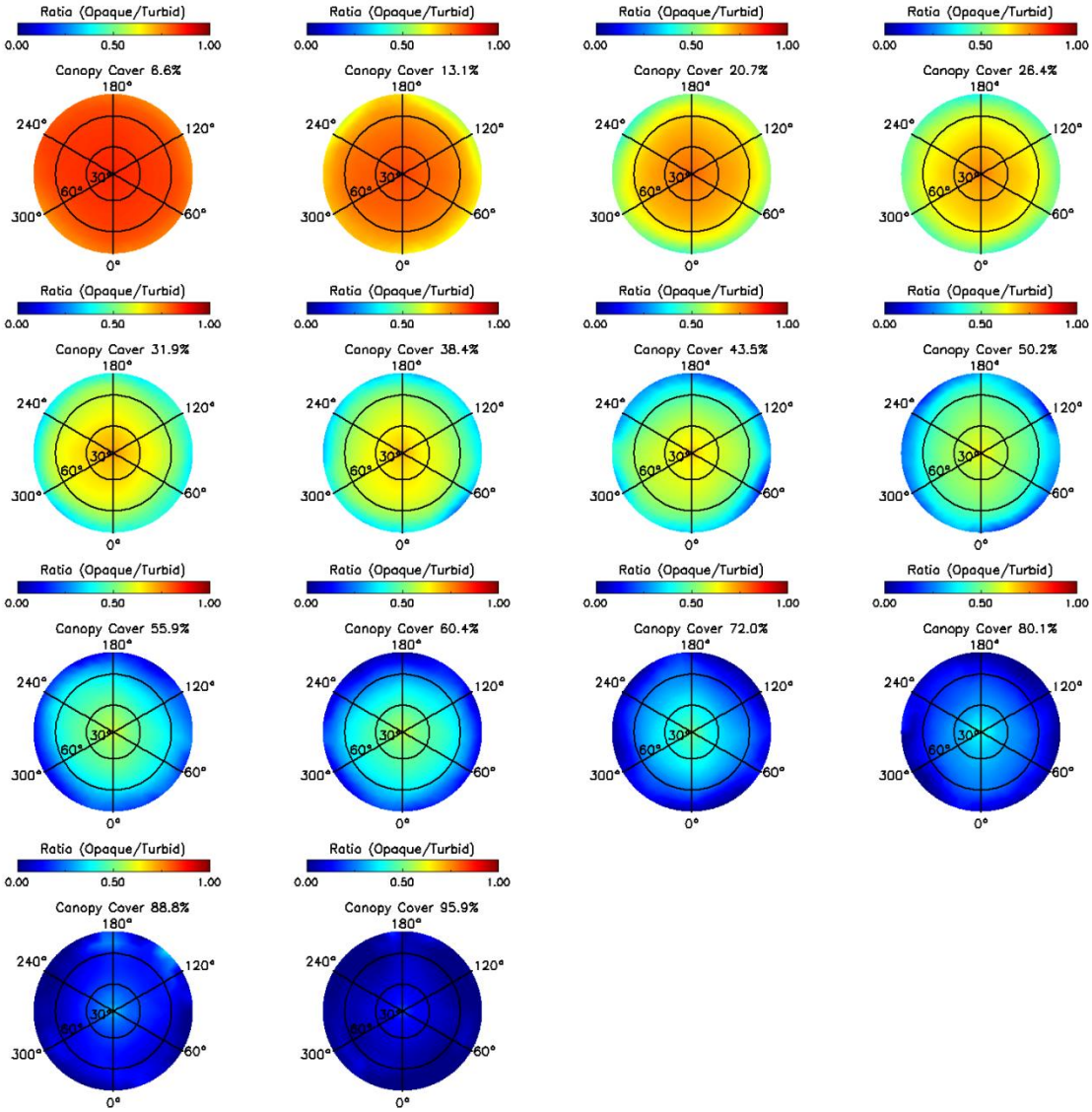

Figure 6: Ratio of the surface fire FRP retrieved when the vegetation canopy viewed through is assumed to be opaque and a turbid media, expressed for different viewing directions and different percentage canopy covers. The difference between the opaque and turbid medium simulations decreases with both view zenith angle and canopy cover.

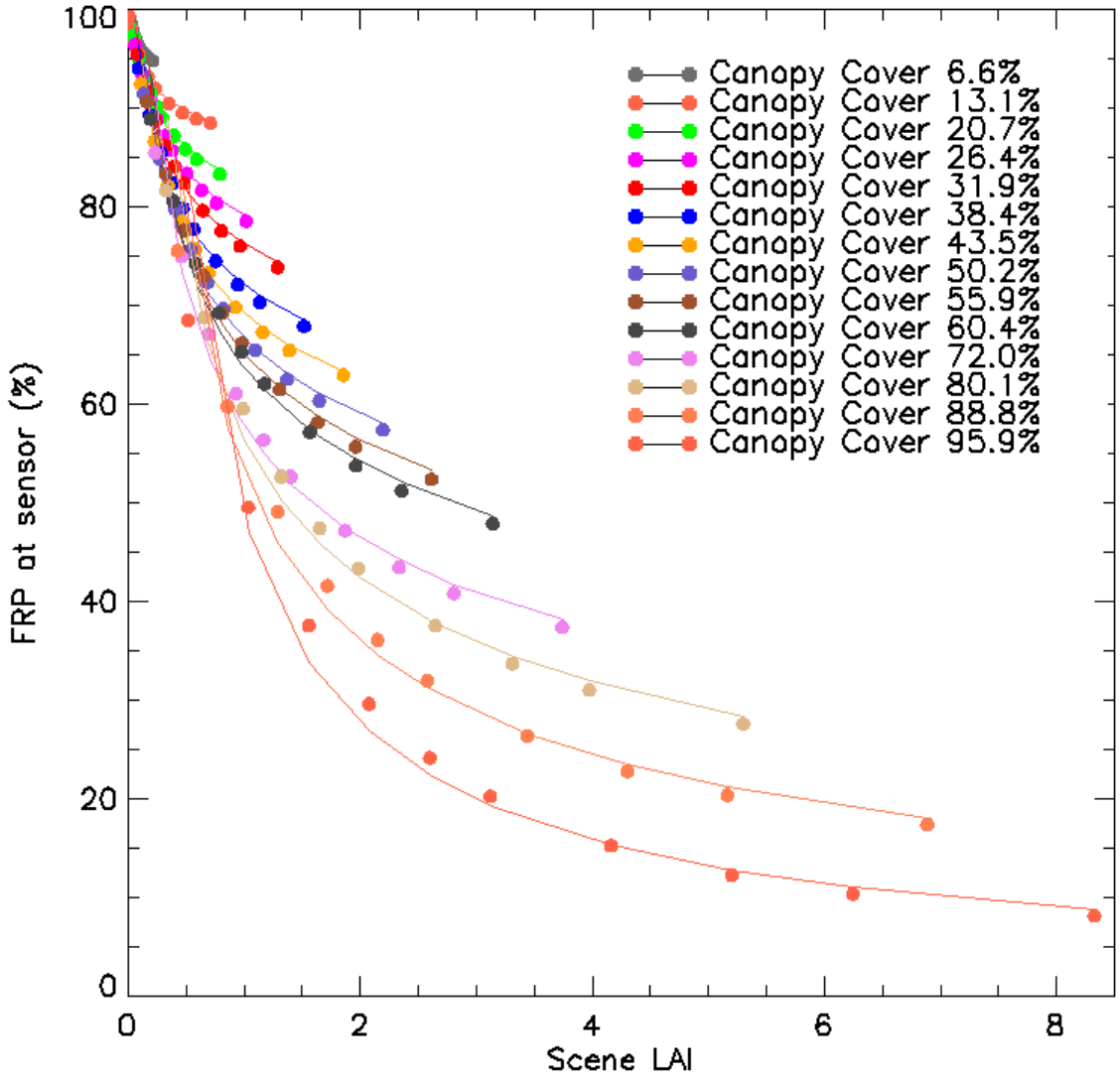

1160

1161 Figure 7: The amount of surface fire FRP retrieved through the canopy, expressed as
1162 a function of scene LAI for different percentage canopy covers. FRP is expressed as a
1163 percentage of that retrieved in the 'no canopy' situation by the same sensor observing
1164 with the same viewing geometry, and the relationships are fitted with best fit 2nd
1165 order polynomial.

1166

1167

1168

1169

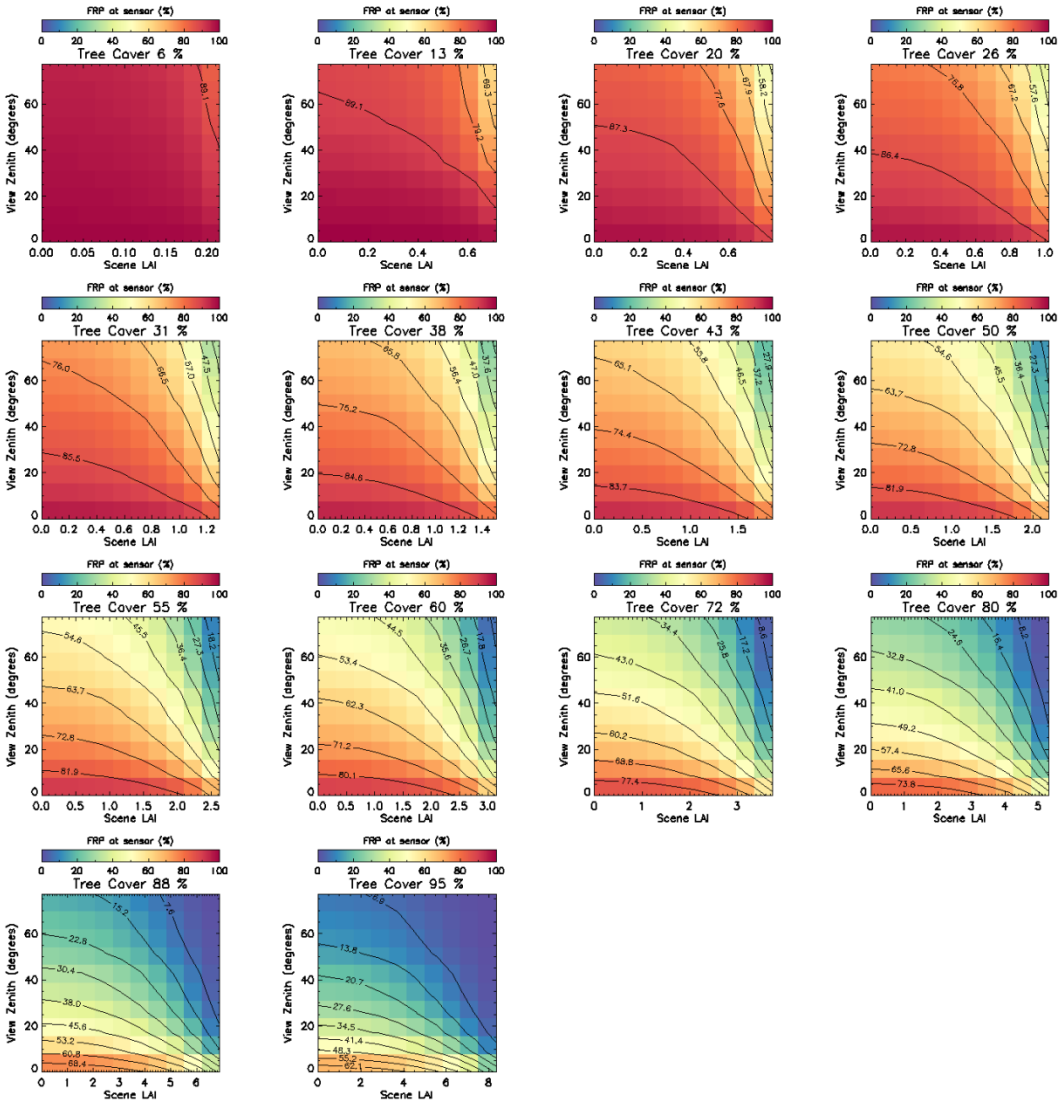

Figure 8: FRP retrieved through the canopy and expressed as a percentage of that retrieved in the 'no canopy' situation by the same sensor observing with the same viewing geometry, and shown as a function of view zenith angle and scene LAI for different percentage canopy covers

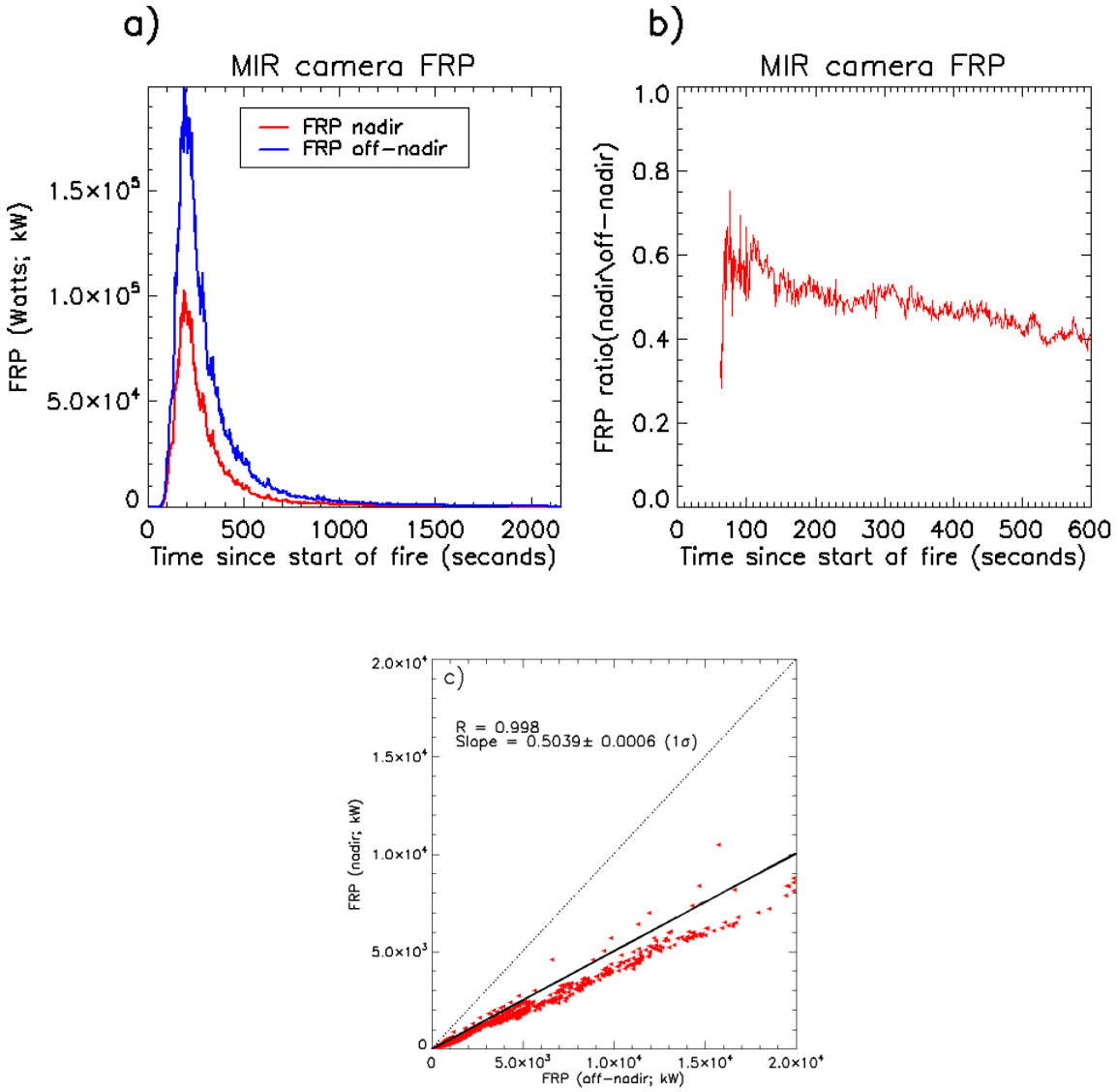

Figure 9: a) Timeseries of nadir and off-nadir FRP retrievals (kW) of a small experimental fire where the nadir camera view was obscured by pine needles and branches (53.5% vegetation cover) and b) the temporal variation in the ratio between the obscured and unobscured camera FRP. c) Scatter plot of the FRP retrieved by the obscured (nadir) and unobscured (off-nadir) thermal cameras for an experimental fire.

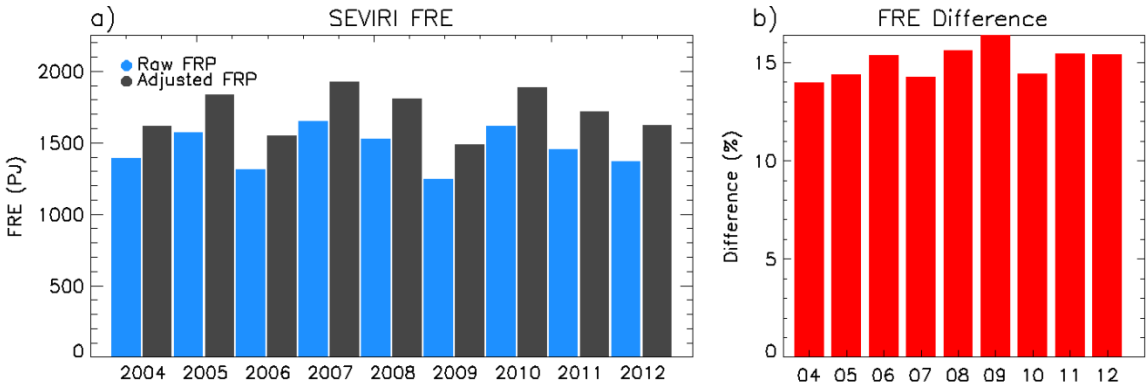

Figure 10: Times series of annual SEVIRI FRE and annual FRE adjusted for canopy interception using percentage tree cover and MODIS LAI estimates (a) and the percentage difference between these two FRE estimates (b).

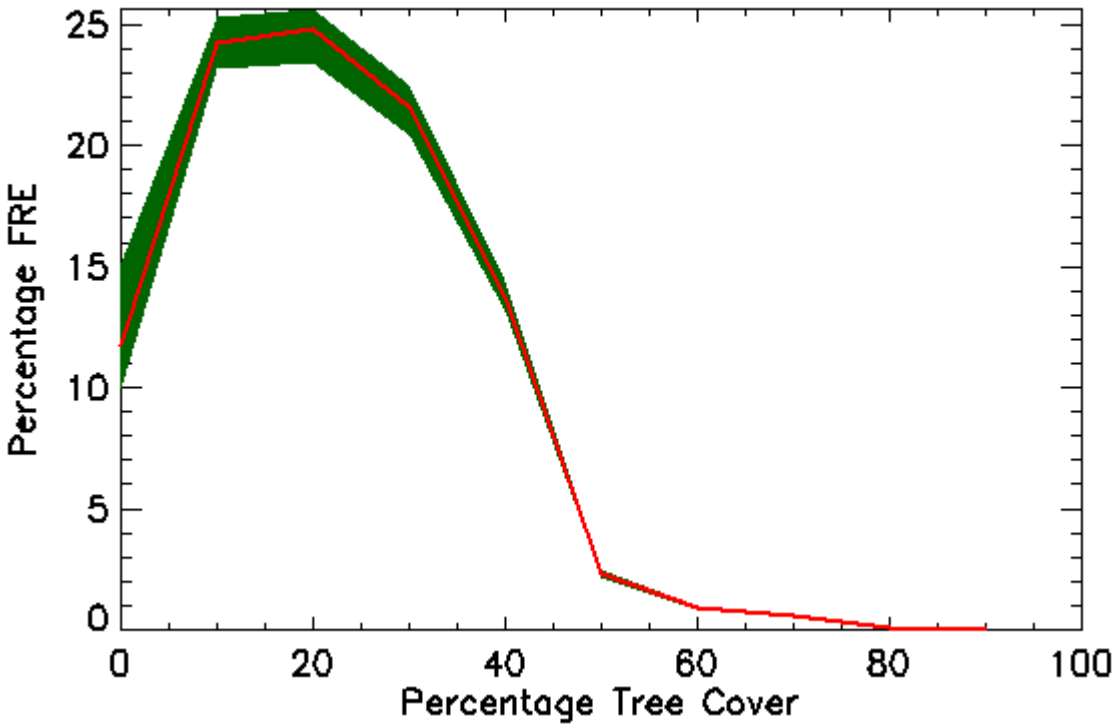

Figure 11: Percentage of SEVIRI FRE (2004-2012) estimated within different percentage tree cover regions (10% bins). The red line indicates the mean percentage of annual FRE whilst the green shaded area indicates the minimum and maximum percentage SEVIRI FRE between 2004 and 2016.